

UNIVERSIDADE FEDERAL DE SÃO CARLOS
CENTRO DE CIÊNCIAS EXATAS E DE TECNOLOGIA
DEPARTAMENTO DE ENGENHARIA MECÂNICA

JOÃO HENRIQUE SCHIAVON MOTA

**TOOL HOLDER INSTRUMENTATION FOR DIDACTIC PURPOSES:
A THEORETICAL AND EXPERIMENTAL APPROACH**

SÃO CARLOS
2023

JOÃO HENRIQUE SCHIAVON MOTA

**TOOL HOLDER INSTRUMENTATION FOR DIDACTIC PURPOSES:
A THEORETICAL AND EXPERIMENTAL APPROACH**

Trabalho de Conclusão de Curso apresentado ao Departamento de Engenharia Mecânica da Universidade Federal de São Carlos, para obtenção do título de Bacharel em Engenharia Mecânica.

Orientador: Prof. Dr. Armando Ítalo Sette Antonialli

SÃO CARLOS
2023



FUNDAÇÃO UNIVERSIDADE FEDERAL DE SÃO CARLOS

COORDENAÇÃO DO CURSO DE ENGENHARIA MECÂNICA - CCEMec/CCET

Rod. Washington Luís km 235 - SP-310, s/n - Bairro Monjolinho, São Carlos/SP, CEP 13565-905
Telefone: (16) 33519703 - <http://www.ufscar.br>

DP-TCC-FA nº 24/2023/CCEMec/CCET

Graduação: Defesa Pública de Trabalho de Conclusão de Curso

Folha Aprovação (GDP-TCC-FA)

FOLHA DE APROVAÇÃO

JOÃO HENRIQUE SCHIAVON MOTA

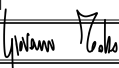
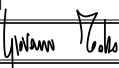
TOOL HOLDER INSTRUMENTATION FOR DIDACTIC PURPOSES: A THEORETICAL AND EXPERIMENTAL APPROACH

Trabalho de Conclusão de Curso

Universidade Federal de São Carlos – Campus São Carlos

São Carlos, 24 de maio de 2023

ASSINATURAS E CIÊNCIAS

Cargo/Função	Nome Completo
Orientador	Armando Ítalo Sette Antonialli
Membro da Banca 1	Giovanni Totis 
Membro da Banca 2	Mariano Eduardo Moreno 



Documento assinado eletronicamente por **Armando Italo Sette Antonialli, Docente**, em 24/05/2023, às 10:18, conforme horário oficial de Brasília, com fundamento no art. 6º, § 1º, do [Decreto nº 8.539, de 8 de outubro de 2015](#).



Documento assinado eletronicamente por **Mariano Eduardo Moreno, Docente**, em 24/05/2023, às 10:20, conforme horário oficial de Brasília, com fundamento no art. 6º, § 1º, do [Decreto nº 8.539, de 8 de outubro de 2015](#).



A autenticidade deste documento pode ser conferida no site <https://sei.ufscar.br/autenticacao>, informando o código verificador **1042311** e o código CRC **686139CE**.

Referência: Caso responda a este documento, indicar expressamente o Processo nº 23112.015680/2023-07

SEI nº 1042311

ACKNOWLEDGMENTS

First I would like to thank my advisor, Prof. Armando Antonioli, who opens the science's doors for me in 2019 and since then has been by my side orienting me in experimental sciences path. Thanks for all the patience, for the best advices, and for the friendship, in this work and in previous ones.

I would like to thank to Prof. Mariano Moreno, who helped me with part of the development of this work.

In special, thanks to my parents, Adriana Maria Schiavon Mota and João Mota, and to my sister Aline Fernanda Mota, who have always supported me to follow my dreams and always did what they could to help me.

I would like to thank to the technical staff of the mechanical manufacturing laboratory, Djalma Durici and Leonildo Pivoto, who helped me with the experimental tests of this thesis and previous works. Thanks also to Heitor Mercaldi who welded the strain gauges for this work.

I would like to thank to all members of the research group “Pesquisa em Manufatura Inteligente” for the support and help in the experimental tests.

I would like to thank my girlfriend, Bruna Vernaschi, for all the patience and support during the elaboration of this thesis.

This thesis also represents the ending of college period, which the conclusion was only possible due to the help of my friends who I would like to thank. Felipe Neves, Igor Marinho, Gabriela Assagra, Guilherme Norri, Maria Bertazzo, Mariana Freitas, Laís Xavier, Lucas Carnevalli, Talia Gibim, Victor William and Vitor Corso, thanks for all friendship and support!

I also would like to thank my professor and friend, Prof. João Vitor Fontes, who always supported me to follow the scientific career and always helped me in the tough path of mechanical engineering.

During the 5 years of undergraduation I lived in two places with many dear people who I would like to thank for the experience, learnings and friendship. Thanks to all residents of the fraternities “Cortição”, from Barão Geraldo, and “Presidente Bernardes” from São Carlos.

Thanks also to all my friends from my hometown, who always supported me and motivated me in this journey.

Finally I acknowledge DEMec, CCET, and UFSCar for the infrastructure and FAPESP for the financial support in three years of scholarship research (process 2019/09381-3).

“An expert is a person who has made all the mistakes that can be made in a very narrow field.” - Niels Bohr.

ABSTRACT

In machining processes the feed and cut movement are the main responsible for the power consumption, justifying a deep study about it in mechanical engineering courses. The power consumption is due to the machining forces involved in these movements, related with the cutting parameters and cutting tool geometry. This relation is usually presented in machining class in a theoretical form, being made through the Orthogonal cutting theory, the Merchant's model and the Kienzle's model for cutting forces. This thesis first present these three theories, and aiming to provide an experimental activity for the machining classes, presents the design and instrumentation of a tool holder for measurement of machining forces. Both tool holder design and instrumentation, are present with an integrative look with other subjects of the mechanical engineering course, approaching mainly the use of materials mechanics. The tool holder was validate numerically and experimentally, pointing to a convergence between results obtained by both ways.

Keywords: Machining, force measurement, cutting theories.

RESUMO

Nos processos de usinagem o movimento de avanço e de corte são os principais responsáveis pelo gasto energético, justificando um profundo estudo quanto a isso nos cursos de engenharia mecânica. O gasto energético é resultado das forças de usinagem envolvidas nesses movimentos, relacionadas com os parâmetros de corte e geometria da ferramenta de corte utilizada. Essa relação é geralmente apresentada nas aulas de usinagem de forma teórica, sendo feita através da Teoria do corte ortogonal, modelo de Merchant e modelo de Kienzle's para forças de corte. Essa dissertação apresenta primeiramente essas três teorias, e visando prover uma atividade experimental para as aulas de usinagem, apresenta o projeto e a instrumentação de um porta ferramenta para a medição de forças de usinagem. Tanto seu projeto quanto sua instrumentação são apresentados com um olhar integrativo com outras disciplinas do curso de engenharia mecânica, abordando principalmente o uso de mecânica dos sólidos. O porta ferramenta foi validado tanto numericamente quanto experimentalmente, obtendo uma convergência entre os resultados obtidos pelas duas formas.

Palavras-chave: Usinagem, medição de força, teorias de corte.

LIST OF FIGURES

Figure 1 – Tool surfaces. a) Shaping process; b) Turning process.	24
Figure 2 – Machining directions. a) Shaping process; b) Turning process.	25
Figure 3 – Tool planes. a) Shaping process; b) Turning process.	26
Figure 4 – Tool angles. a) Shaping process; b) Turning process.	27
Figure 5 – Diagram of the cutting process.	29
Figure 6 – Machining forces and parameters, for the turning process. Note that the cutting velocity \vec{v}_c has the same direction than the cutting force \vec{F}_c	30
Figure 7 – Forces involved in the chip formation.	31
Figure 8 – THALES circle.	32
Figure 9 – Exploded view of the cutting setup assembly.	36
Figure 10 – Graphic representation of the tool holder design.	36
Figure 11 – Tool holder in the experimental setup.	37
Figure 12 – Visualization of stress and strain in a body: a) Force being applied to a perpendicular and a parallel area; b) Relative displacement while a force is applied to a body.	38
Figure 13 – Rotation of reference frame in a point under normal and shear stress. Rotation of θ rad in the anti clockwise direction.	40
Figure 14 – Cantilever beam under a bending force and a compression force.	41
Figure 15 – Wheatstone bridge circuit.	42
Figure 16 – Grid of strain Gauge 1-XY41-3/350.	44
Figure 17 – Schematic representation of the running system of a shaping machining. Points A,B,C,D indicates the link points between the machine elements. Dimensions and elements positions are merely illustrative.	45
Figure 18 – Actual shaping machine used in this work.	46
Figure 19 – Strain gauge placement on tool holder. In blue the tool holder support, in white the tool holder, in red the cutting tool and in grey the bolt for hold the tool.	47
Figure 20 – Tool holder free body diagram. Approached as a cantilever beam.	48
Figure 21 – Mesh and results for the pair of force (5000N, 3250N).	50
Figure 22 – Query curves F,G,H used for the analysis.	50
Figure 23 – Stresses along the back face of tool holder, using a cutting force of 5000N and a feed force of 2000N.The X axis contains the points located in the line F from the Figure 22.	51
Figure 24 – Stresses along the back face of tool holder, using a cutting force of 5000N and a feed force of 3250N.The X axis contains the points located in the line F from the Figure 22.	51

Figure 25 – Strain in the Y direction along the back face of tool holder, using a cutting force of 5000N and a feed force of 2000N. The X axis contains the points located in the line F from the Figure 22.	52
Figure 26 – Strain in the Y direction along the back face of tool holder, using a cutting force of 5000N and a feed force of 3250N. The X axis contains the points located in the line F from the Figure 22.	52
Figure 27 – Strain in the U and V direction along the lateral face of tool holder, using a cutting force of 5000N and a feed force of 2000N. The X axis contains the distance to the bottom from the points located in the lines G and H from the Figure 22.	53
Figure 28 – Strain in the U and V direction along the lateral face of tool holder, using a cutting force of 5000N and a feed force of 3250N. The X axis contains the distance to the bottom from the points located in the lines G and H from the Figure 22.	53
Figure 29 – Strain in the Y direction along the front face of tool holder, using a cutting force of 5000N and a feed force of 2000N. The X axis contains the points located in a line parallel to F line from the Figure 22, but located in the front face from the tool holder.	54
Figure 30 – Strain in the Y direction along the front face of tool holder, using a cutting force of 5000N and a feed force of 3250N. The X axis contains the points located in a line parallel to F line from the Figure 22, but located in the front face from the tool holder.	55
Figure 31 – Graphic representation of the workpiece.	56
Figure 32 – Diagram of cutting parameters combinations possible. Diagram available in the own machine.	57
Figure 33 – Correction curve for strain calibration: a) Expected and obtained curves for front face strain gauge; b) Expected and obtained curves for back face strain gauge. Tool NEG2.	60
Figure 34 – Correction curve for strain calibration: a) Expected and obtained curves for front face strain gauge; b) Expected and obtained curves for back face strain gauge. Tool NEG1.	61
Figure 35 – Correction curve for strain calibration: a) Expected and obtained curves for front face strain gauge; b) Expected and obtained curves for back face strain gauge. Tool NEU0.	61
Figure 36 – Correction curve for strain calibration: a) Expected and obtained curves for front face strain gauge; b) Expected and obtained curves for back face strain gauge. Tool rake angle γ_o : 5°.	62

Figure 37 – Correction curve for strain calibration: a) Expected and obtained curves for front face strain gauge; b) Expected and obtained curves force back face strain gauge. Tool rake angle γ_o : 8.6°	62
Figure 38 – Active forces measured. Each bar represents a feed f . a) Cutting force \vec{F}_c ; b) Feed force \vec{F}_f	64
Figure 39 – Active force \vec{F}_a measured.	65
Figure 40 – Cutting force \vec{F}_c (refereed as “horizontal force” by authors) and feed force \vec{F}_f (refereed as “vertical force” by authors) versus the clearance angle α_o (refereed as “relief angle” by authors). a) Cutting force \vec{F}_c ; b) Feed force \vec{F}_f . (i) $h = 0,05\text{mm}$, $V_c = 48,6\text{m/min}$, $\gamma_o = 15^\circ$; (ii) $h = 0,1\text{mm}$, $V_c = 36\text{m/min}$, $\gamma_o = 15^\circ$; (iii) $h = 0,2\text{mm}$, $V_c = 26,4\text{m/min}$, $\gamma_o = 15^\circ$	66
Figure 41 – Active forces measured versus uncut chip thickness h . a) Cutting force \vec{F}_c ; b) Feed force \vec{F}_f	67
Figure 42 – Neutral tool Wear due to build-up edge formation.	68
Figure 43 – Linearized forces for the Kienzle’s constants determination.	69

LIST OF TABLES

Table 1 – Strain Gauge 1-XY41-3/350 resistance and dimensions.	43
Table 2 – FEM Setup.	49
Table 3 – Tools used in the tests.	56
Table 4 – Cutting parameters.	57
Table 5 – Lever lengths.	57
Table 6 – Number of samples per variables combination. Cutting speed v_c , depth of cut a_p , and cutting edge angle κ_r were not changed.	58
Table 7 – Comparison between measured strains and simulation strains. Assembly with neutral tool.	63
Table 8 – Shear angle Φ per variables combination.	68
Table 9 – Kienzle’s constants experimentally determined for the neutral tool. . . .	68

LIST OF ABBREVIATIONS AND ACRONYMS

ABNT	Associação Brasileira de Normas Técnicas
CCET	Centro de Ciências Exatas e de Tecnologia
DEMec	Departamento de Engenharia Mecânica
FAPESP	Fundação de Amparo à Pesquisa do Estado de São Paulo
FEM	Finite Element Method
UFSCar	Universidade Federal de São Carlos

LIST OF SYMBOLS

P_r	Reference plane
P_F	Working plane
κ_r	Cutting edge angle
γ_o	Rake angle
\vec{F}_c	Cutting force
\vec{F}_f	Feed force
\vec{F}_p	Passive force
α_o	Clearance angle
f	Feed
a_p	Depth of cut
v_c	Cutting velocity
b'	Chip width
b	Uncut chip width
Φ	Shear angle
A	Cutting edge point / Arbitrary point / Point on the cantilever beam surface / Shaping machine pivot point
B	Chip flexion point / Arbitrary point / Point on the cantilever beam surface / Shaping machine pin
h	Uncut chip thickness
h'	Chip thickness
v_{ch}	Chip speed
A'_{ch}	Cross section area of chip
A_{ch}	Cross section area of uncut chip
\vec{F}_{rn}	Normal rake force
\vec{F}_{rt}	Friction rake force

μ	Friction coefficient
τ_{Φ}	Chip mean shear stress
\vec{F}_{Φ}	Chip shear force
$\vec{F}_{\Phi n}$	Chip normal force
β	Angle between normal rake force and active force
ξ	Angle between chip shear force and active force
P	Machine power consumption
A_1	First Zvorykin constant
A_2	Second Zvorykin constant
θ	Chip inclination angle / Rotation angle
K_s	Specific cut pressure
$k_{s,1}$	Specific cut pressure for uncut chip thickness equals to 1mm
z	Cutting force gradient
$k_{f,1}$	Specific cut pressure for uncut chip width equals to 1mm in the feed direction
x	Cutting force gradient in the feed direction
\vec{F}	Any force
A	Any area
$\vec{\sigma}$	Normal stress
$\vec{\tau}$	Average shear stress
A_n	Area perpendicular to a force
A_t	Area parallel to a force
L_i	Initial distance between two random points inside a body
L_f	Final distance between two random points inside a body
ϵ	Normal strain
E	Elastic modulus

γ	Shear strain
G	Shear modulus
ν	Poison's ratio
ϵ_y	Strain perpendicular to stress direction
ϵ_x	Strain parallel to stress direction
σ_z	Stress in an arbitrary Z direction, perpendicular to Y direction
σ_y	Stress in an arbitrary Y direction, perpendicular to Z direction
τ_{zy}	Shear stress in arbitrary directions Y and Z / Shear stress in the lateral strain gauge grid
σ'_z	Stress in an arbitrary Z' direction, perpendicular to Y' direction
σ'_y	Stress in an arbitrary Y' direction, perpendicular to Z' direction
τ'_{zy}	Shear stress in arbitrary directions Y' and Z'
ϵ_z	Strain in an arbitrary Z direction, perpendicular to Y direction / Strain in Z direction in the tool holder face
ϵ_y	Strain in an arbitrary Y direction, perpendicular to Z direction / Strain in Z direction in the tool holder face
γ_{zy}	Shear strain in arbitrary directions Y and Z / Shear strain in the lateral strain gauge grid
ϵ'_z	Strain in an arbitrary Z' direction, perpendicular to Y' direction
ϵ'_y	Strain in an arbitrary Y' direction, perpendicular to Z' direction
γ'_{zy}	Shear strain in arbitrary directions Y' and Z'
\vec{F}_N	Compression force
\vec{F}_B	Bending force
L_Y	Distance between arbitrary points in a cantilever and plane of force application / Cutting force lever length to the strain gauges position
π	Plane dividing a cantilever beam in a half
ζ	Plane dividing a cantilever beam in a half, perpendicular to Π
t	Cantilever beam thickness

c	Cantilever beam width
σ_A	Normal stress in Y direction on point A from the cantilever beam
τ_B	Normal stress in Z direction on point B from the cantilever beam
M	Total moment acting in the neutral axis
d_A	Distance from point A to neutral axis
I	Moment of inertia of cantilever cross section
A_c	Area of cantilever cross section
σ^A	Total stress in Y direction on point A
R	Resistance
U	Voltage
i	Current passing through the resistor
L_r	Resistor length
A_r	Area of resistor cross section
ρ	Resistor resistivity
V	Voltage supply in a wheatstone bridge circuit
R_1, R_2, R_3, R_4	Resistors in a wheatstone bridge circuit
ΔV	Voltage reading in a wheatstone bridge circuit
k	Gauge factor of a strain gauge
ϵ_{R1}	Strain of strain gauge 1
ϵ_{R2}	Strain of strain gauge 2
C	Shaping machine pivot point
D	Shaping machine pin
X	Direction perpendicular to the shaping machine working plane
Y	Vertical direction
Z	Feed direction
U	Z direction rotated by 45° in anti-clockwise direction around X axis

V	Y direction rotated by 45° in anti-clockwise direction around X axis
ϵ_u	Strain in U direction
ϵ_v	Strain in V direction
σ_{SGZ-}	Normal stress in Y direction in the back face strain gauge grid
τ_{SGX-}	Shear stress in Z direction in the lateral face strain gauge grid
L_Z	Feed force lever length to the strain gauges position
D_{SGX-}	Distance from the lateral face strain gauges to the tool holder bottom
D_{SGZ-}	Distance from the back face strain gauges to the tool holder bottom

SUMMARY

1 – INTRODUCTION	21
1.1 Goals	22
1.2 Text Structure	22
2 – THEORETICAL APPROACH	23
2.1 Reference systems	23
2.1.1 Tool surfaces	24
2.1.2 Tool directions	24
2.1.3 Tool planes	25
2.1.4 Tool angles	26
2.2 Orthogonal cutting theory	28
2.2.1 Shear plane model	28
2.2.2 Chip speed	29
2.3 Merchant’s model	29
2.3.1 Machining forces	29
2.3.2 Chip shearing	30
2.3.3 Shear angle determination	32
2.4 Kienzle force model	33
3 – EXPERIMENTAL APPROACH	35
3.1 Tool holder design	35
3.2 Force measurement	36
3.2.1 Force, stress and strain	37
3.2.2 Strain gauge	42
3.2.3 Modelling with strain gauge	44
3.2.4 FEM validation	48
3.3 Experimental setup	55
3.3.1 Workpiece	55
3.3.2 Cutting Parameters	56
3.3.3 Data acquisition	58
4 – RESULTS	63
4.1 Strain convergence	63
4.2 Active machining forces	64
4.3 Shear angle and Kienzle’s constants	67
5 – CONCLUSION	70

5.1 Future works	70
REFERENCES	71

1 INTRODUCTION

The mechanical engineering bachelor's degree intends to provide to its students a solid formation at the areas of machine design, machine dynamics, manufacturing processes, mechatronics concepts and fluid and thermal machines, beyond essentials society subjects such as business management, environmental development, interpersonal relations, etc., as described by the Pedagogical Project of Mechanical Engineering from Federal University of São Carlos (UFSCAR, 2013).

Within the technical courses, the manufacturing processes chain shows itself as complementary and essential for others subjects: A machine design needs to consider the available fabrication processes for its manufacture, considering the dynamics of each process. The same principle applies to mechatronic projects, a good project has a feasible assembly. About fluids and thermal machines their fabrication processes are directly related to their efficiency, due to the material and surface roughness.

Among the manufacturing processes studied in the mechanical engineering undergraduate course (casting, forging, prototyping, machining, etc.), the main group regards to the machining processes, due to their popularity in the industries, to the surface quality that they provide and the ease working with metal alloys (FERRARESI, 1970). This importance provides an exclusive subject for machining studies inside the pedagogical project of mechanical engineering bachelor's.

The technical standard DIN8580 (2003) defines machining as all processes which transform the geometry and mass of some material through the cut. Cut a material can be a process very complicated, to perform this task correctly it is necessary knowledge of materials mechanics, dynamics, and thermal conductivity; To verify the quality of the cutting process, the knowledge of instrumentation it is essential, beyond the data acquirement and statistical concepts.

Clarified the union between the machining studies with other areas of the mechanical engineering bachelor's, it is evident the possibility of an integrating teaching in the machining subject. This way, this monograph intend to present the development of the design and instrumentation of a tool holder, able to measure the active cutting forces, for experimental activities in the machining subject, approaching also other areas from the bachelor's. To validate the instrumentation and design of the tool holder, experimental tests were performed aiming to determinate these forces, based in some of machining theories.

In order to establish the reader about these theories, this monograph will present the current theories regarding the forces involved in the cutting process: The orthogonal cutting theory, the Merchant's circle and the Kienzle's model. This theoretical approach also intends to be didactic in nature.

All quantities present in this work are measured in the international system, excepts for distance, area, speed and stress which are respectively in mm, mm², m/min and in MPa.

1.1 Goals

As pointed, this work aim to touch different areas from mechanical engineering with a didactic and integrated look for it. This main goal is divided by the following sub goals:

- Theoretical presentation about the cutting processes: Presents the orthogonal cutting theory, Merchant's model, Kienzle's model;
- Design of a tool holder able to validate the theories presented;
- Numerical validation of the tool holder;
- Numerical validation of the tool holder analytical model;
- Experimental validation of the tool holder: Measure the active cutting forces;
- Experimental validation of the cutting theories: Determinate the shear angles and Kienzle's constants.

1.2 Text Structure

Defined the goals of this work, this monograph is structured in the following way:

- Theoretical Approach - Presents the theory behind the forces acting in a machining process;
- Experimental Approach - Presents the development and instrumentation of the tool holder and the experimental tests performed;
- Results - Presents the results of the experimental tests and compare it to the theory;
- Conclusion - Presents an analysis about the results.

2 THEORETICAL APPROACH

In order to establish the best techniques for machining processes, several theories about the cutting procedure, regarding forces, dynamics, thermal loads, etc, have been developed. To perform the propose of this work, the development and instrumentation of a tool holder for the teaching of machining classes, the study and review of the classical theories approaching the machining forces were essentials and will be presented in this chapter.

First of all it is necessary narrow the machining field which will be studied. The technical standard DIN8589 (2003) divides the machining processes in two main groups, the ones which uses tools with defined geometry, and the ones which uses tools without a defined geometry. This monograph works with the first group, which can be divided in three subgroups: Processes with free and orthogonal cuts; Processes with free and diagonal cuts; And processes with bound and diagonal cuts (KLOCKE, 2013). Again, this work is restricted to the first group.

Defined the type of process studied here, three theories predominates in determining the relation between the cutting forces, chip formation, cutting parameters and tool geometry: The orthogonal cutting theory, the Merchant's model and the Kienzle force model. The first two theories are complementary to each other, and the Kienzle force model is a general model for the cutting force determination, being applicable for an orthogonal cut, as discussed below. This chapter first presents a brief introduction to the reference systems used in the machining studies, in order to facilitate the reader abstraction about the positions and angles addressed in these theories.

2.1 Reference systems

For an easy visualization of the planes, angles, and directions covered in the theories used in this work, the used reference system will be discussed in this section, focused in the planes of interest. There are two standardized reference systems, the *tool-in-hand system* and the *tool-in-use system*. This thesis uses the first system, hence the second system will not be presented here.

The system and its planes will be presented using two processes as examples: The turning process, due to it popularity among the machining process, and the shaping process, since this is the process used in this work. Before the explanation about the reference system it is important to evidence the differences between these process: Whereas in the turning process the workpiece is in movement (rotational movement, specifically) and the tool is steady regarding the cutting movement, at the shaping process the workpiece is steady, regarding the cut movement, and the tool is in movement (linear movement,

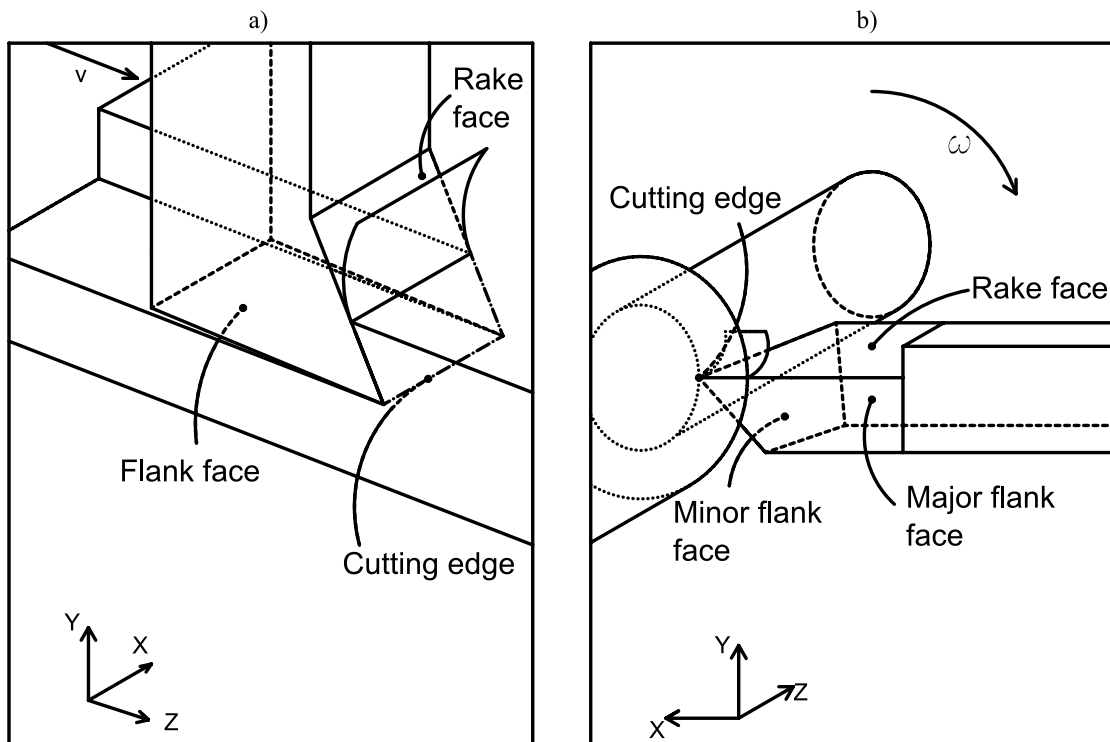
specifically). Another difference is the constant cutting in the turning (and hence a constant feed) whereas in the shaping the cut is intermittent, such as the feed rate.

Even with this differences in it kinematics, the standardization of the tools geometries and reference systems can be used for both processes. The following subsections shows the application of the technical standard NBR ISO 3002-1 from Associação Brasileira de Normas Técnicas (ABNT) (2013) in these processes, which is based considers the workpiece as the inertial framework.

2.1.1 Tool surfaces

For this work some surfaces of the tool are important: The rake face and the flank faces. The edge between these faces defines the cutting edge, where the forces that performs the material cut occur. The rake face is the face where the chip slides before it completes rupture from the workpiece, and the flank faces are the faces that pass above the workpiece surface already machined. The Figure 1 shows these surfaces.

Figure 1 – Tool surfaces. a) Shaping process; b) Turning process.



Source: Author.

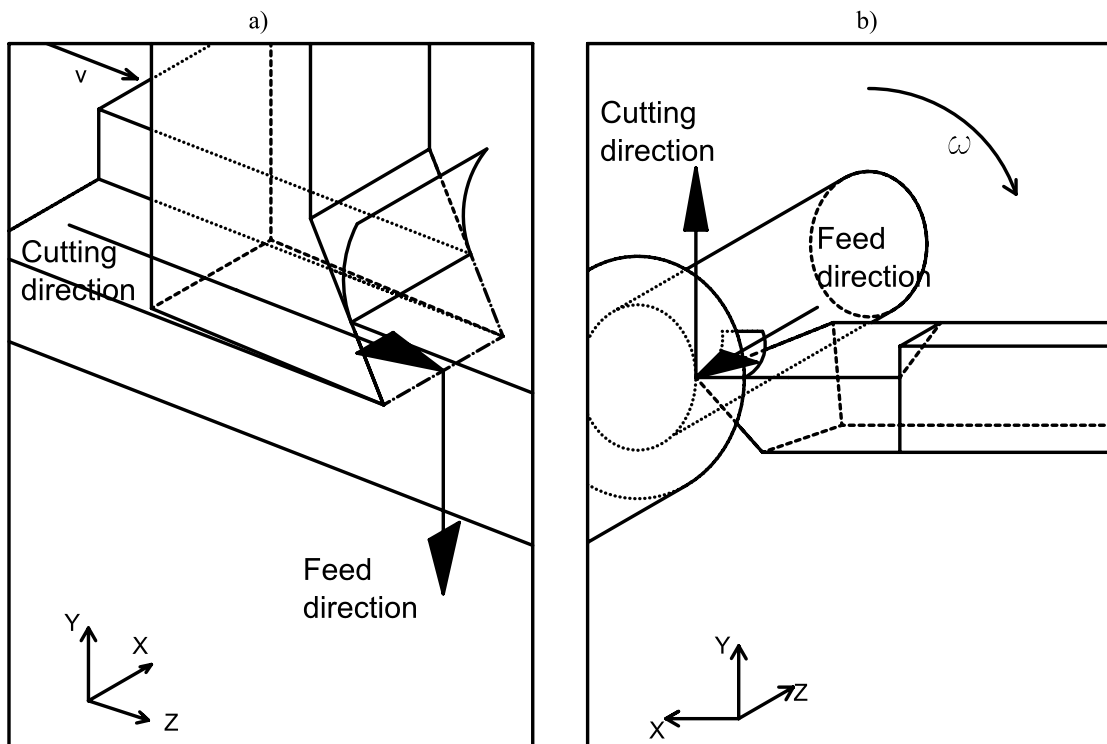
2.1.2 Tool directions

To determinate the planes and forces involved in the processes it is necessary to determinate some directions. These directions are obtained decomposing the effective

cutting movement, which can be made in two directions: The cutting direction and the feed direction. These directions are shown in the Figure 2.

The cutting force and the feed force are parallel to the cutting direction and the feed direction, respectively, such as it velocities. However, it is important to highlight a caveat: Since the feed movement of the shaping process is intermittent, the NBR ISO 3002-1 points to the non definition of the feed velocity. The cutting force and the feed force, as deeper described below, are also parallel to these directions (Important to highlight both forces and velocities are respectively to the tool in relation to the workpiece).

Figure 2 – Machining directions. a) Shaping process; b) Turning process.



Source: Author.

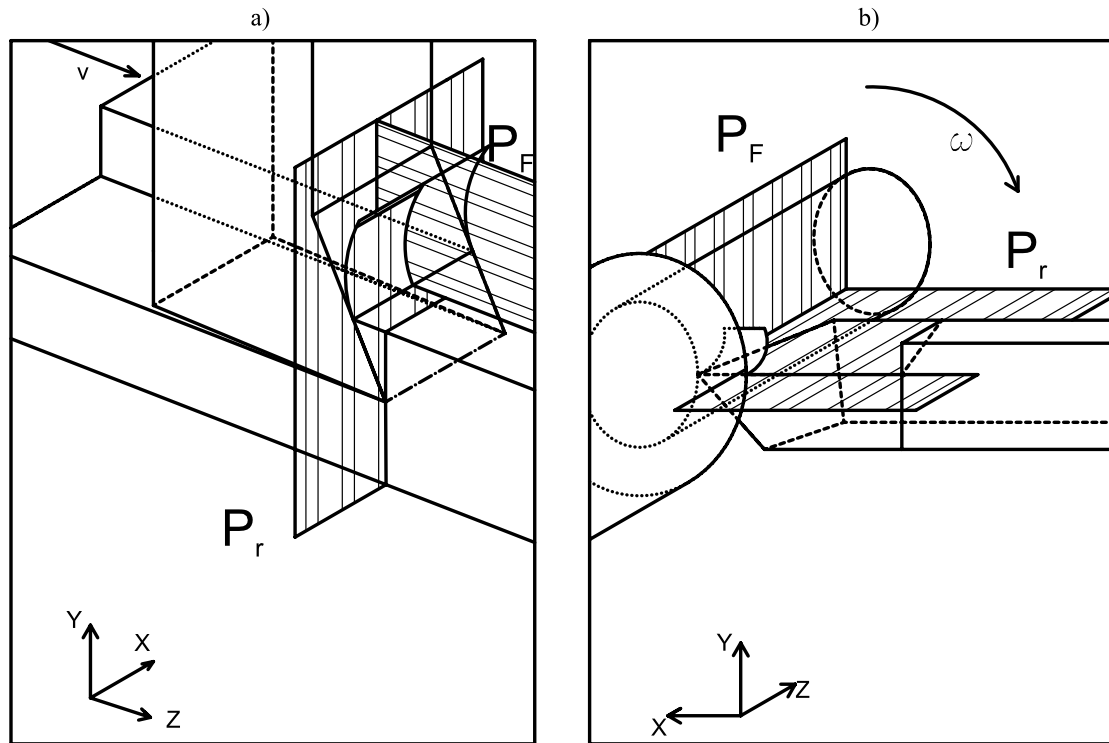
2.1.3 Tool planes

Established the tool surfaces and the machining movements, it is possible to determine few planes according to the NBR ISO 3002-1. The planes presented here are only the necessities to perform of this work.

There are two planes necessary for this study, the tool reference plane P_r and the working plane P_F . The tool reference plane P_r is defined as the plane which contains the cutting edge and it is perpendicular to the cutting direction. The working plane P_F is defined as the plane which contains the cutting and feed direction. These planes are shown in the Figure 3.

Notice that NBR ISO 3002-1 also defines other planes, as the orthogonal plane and normal plane, what for the case of cutting edge angle κ_r equals to 90° and cutting edge belonging to the reference plane, becomes the same plane as the working plane.

Figure 3 – Tool planes. a) Shaping process; b) Turning process.



Source: Author.

2.1.4 Tool angles

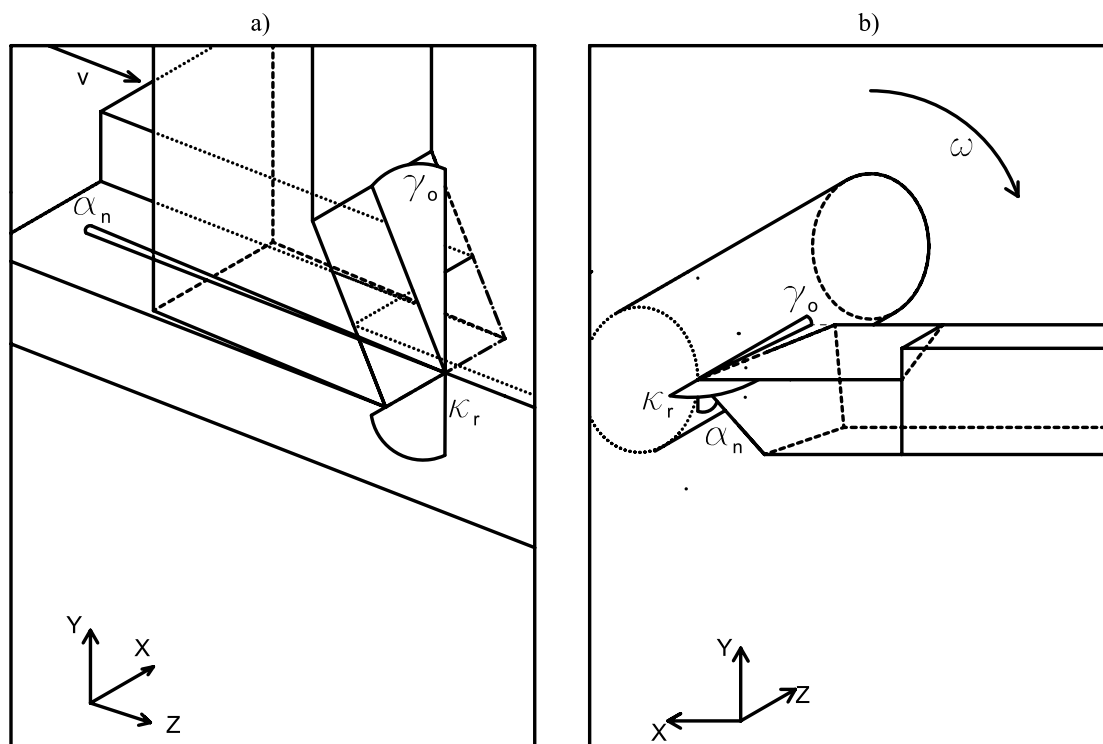
To finish the presentation of the tool geometry, three angles must be shown to be used in the below theories. The first angle is the cutting edge angle κ_r , which is defined as the angle between the cutting edge and the orthogonal plane P_r , measured in the reference plane P_r . The importance of this angle, among other factors, is the relation with the desired workpiece geometry and the active machining forces.

The second angle is the rake angle γ_o , defined as the angle between the rake surface and the reference plane P_r , measured perpendicular in the working plane. Klocke (2013) points out to a direct relation between this angle and the active cutting forces, as an increase of one degree in this angle, the cutting force \vec{F}_c tends to increase by 1,5% while the feed force \vec{F}_f tends to increase by 5%, and the passive force \vec{F}_p by 4%. The decrease of one degree leads to the opposite force behavior. These forces is explained deeper in 2.3.1.

The third angle is the orthogonal clearance angle α_o , defined as the angle between the major flank face and the workpiece, also measured in the working plane. This angle has influence in the tool wear and the workpiece surface quality, and as described by Klocke

(2013), theoretically it does not influence the cutting forces. These three angles are shown in Figure 4.

Figure 4 – Tool angles. a) Shaping process; b) Turning process.



Source: Author.

2.2 Orthogonal cutting theory

In order to study the material cutting processes, the orthogonal cutting theory seeks for a relation between the tool geometry, machining parameters and chip formation, based on the shear plane model. The usual cutting parameters are the feed f - the distance which the tool advances against the workpiece, in the feed direction, measured in mm-, the depth of cut a_p - the distance of the tool stepping over into the workpiece, measured in mm- and the cutting speed v_c - the velocity which the tool realize the cutting in the cutting direction, measured in m/min.

2.2.1 Shear plane model

The relation between the chip formation, machining parameters and tool geometry is obtained considering that all chip deformation occurs in only one plane: The shear plane (Shown in Figure 5), also known as the primary shear zone. This theory is also substantiated in some assumptions, in order to facilitate the model. The assumptions are the following:

- Planar state of strain;
- The tool is enough sharp, with a cutting edge radius close to zero;
- The cutting edge is perpendicular to the working plane;
- The passive force is negligible;
- Constant cutting velocity v_c and depth of cut a_p ;
- The chip width b' is equal to the uncut chip width b ;
- There is no contact between the flank face and the workpiece;
- The chip is continuous;

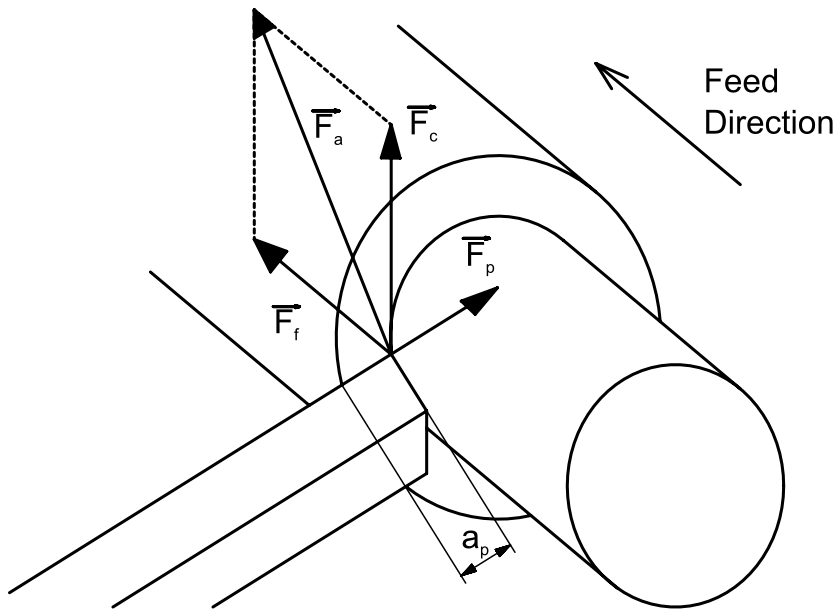
This way it is possible to draw the diagram of Figure 5, representing the cutting process, and from it extract the desired relations. In the figure, which is a view by the working plane, the angle Φ represents the shear angle, the angle between the shear plane of the chip with the machined surface, the point A represents the cutting edge, and the point B the point where the chip starts the deformation. Notice that once the cutting edge angle κ_r is equals to 90° it implies in an uncut chip thickness h equals to the feed f , and uncut chip width b equals to the depth of cut a_p (dimension perpendicular to the working plane).

Based on this representation of the orthogonal cutting, the shear angle Φ can be used to found a relation between the uncut chip thickness h and the deformed chip thickness h' , by joining the Equations 1 and 2, resulting in the Equation 3, where the chip compression factor λ_h is the relation h'/h . This dimensionless value is a representation of the relation between the tool geometry and the chip formation.

$$\sin(\Phi) = \frac{h}{AB} \quad (1)$$

and the active force \vec{F}_a . The active force \vec{F}_a can then be divided in two forces, the cutting force \vec{F}_c and the feed force \vec{F}_f . The active force is responsible for the power consumption of the machine tool, and belongs to the work plane. The passive force \vec{F}_p is perpendicular to the working plane and does not spend power from the machine tool (FERRARESI, 1970). The Figure 6 shows these forces (being applied in the workpiece), and cutting parameters for the turning process. Since it is easy visualised for the shaping process, it is not shown in the figure.

Figure 6 – Machining forces and parameters, for the turning process. Note that the cutting velocity \vec{v}_c has the same direction than the cutting force \vec{F}_c .



Source: Author.

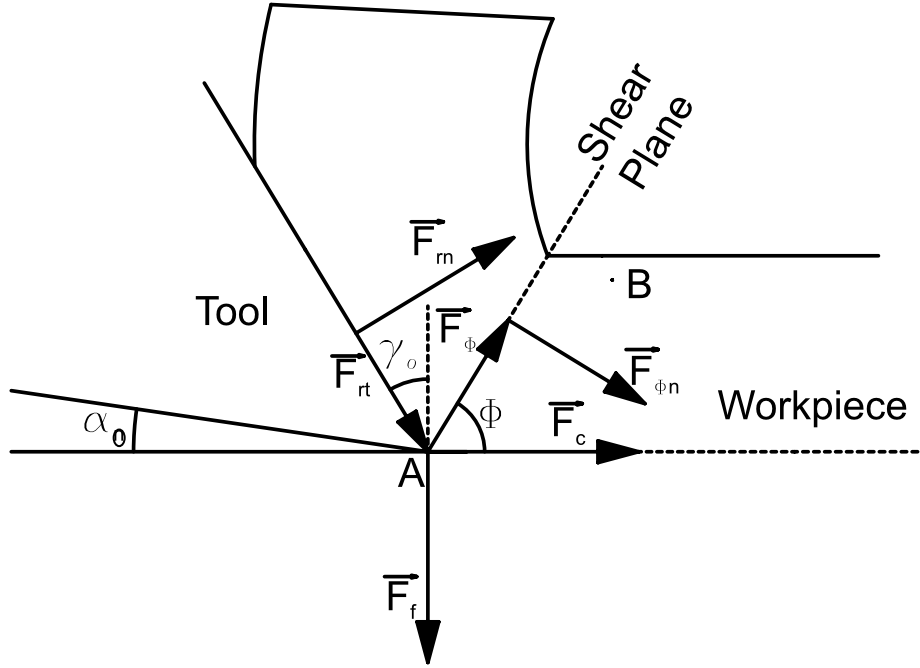
2.3.2 Chip shearing

Considering the orthogonal cutting theory, and hence the nonexistence of passive forces, the force diagram of the Figure 7 can be used to represent the efforts involved in the chip shearing process. In the Figure 7 the force \vec{F}_{rn} and \vec{F}_{rt} are respectively the normal rake force in the chip, being applied by the tool rake face and the friction rake force, also applied by the tool rake face. The region where these forces are applied is known as secondary shear zone. Considering the validity of the Coloumb's law on the rake surface, the ratio $|\vec{F}_{rt}|/|\vec{F}_{rn}|$ is equal to the friction coefficient μ .

Once it is assumed that all the chip deformation occurs only in the shear plane, the chip mean shear stress τ_Φ can be related with the chip shear force \vec{F}_Φ (Also shown in the Figure 7, herein with the chip normal force $\vec{F}_{\Phi n}$ to the shear plane, caused by the chip normal stress), as described by the Equation 5 (Further details about the relation between stress, strain and force are present in 3.2.1).

$$\tau_{\Phi} = \frac{|\vec{F}_{\Phi}|}{A_{ch}/\sin(\Phi)} = \frac{|\vec{F}_{\Phi}| \sin(\Phi)}{bh} \quad (5)$$

Figure 7 – Forces involved in the chip formation.



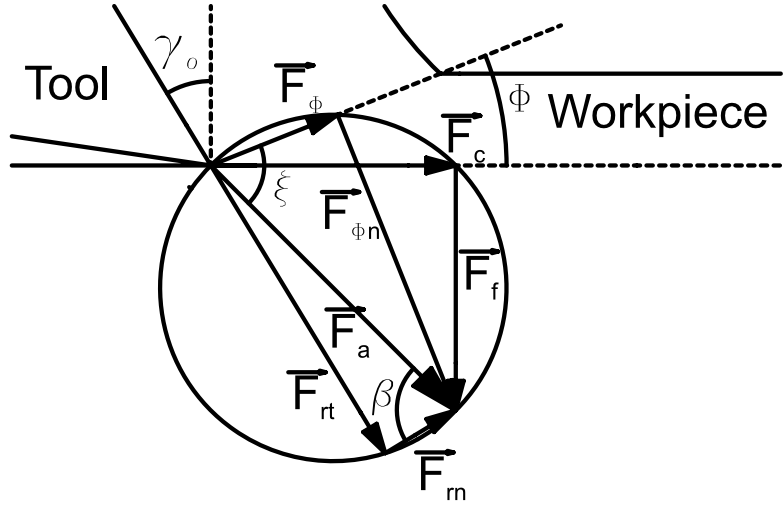
Source: Author.

The forces presented in Figure 7 allows three different forms to write the active machining force \vec{F}_a , as function of the cutting \vec{F}_c and feed force \vec{F}_f , as already presented: $\vec{F}_a = \vec{F}_c + \vec{F}_f$; As function of the normal rake force and friction rake force: $\vec{F}_a = \vec{F}_{rn} + \vec{F}_{rt}$; And as function of the chip shear force \vec{F}_{Φ} and the chip normal force $\vec{F}_{\Phi n}$: $\vec{F}_a = \vec{F}_{\Phi} + \vec{F}_{\Phi n}$. The geometric representation of the active force \vec{F}_a can then be represented by the THALES circle, as shown by the Figure 8, where these forces were translated in order to visualize geometrically the vectorial sum.

Looking to Figure 8 it is easy to see that the angle β it is equal to $\tan^{-1}(\mu)$. The angle ξ is the angle between the active force \vec{F}_a and the chip shear force \vec{F}_{Φ} . Using the advantage of the planar geometry and some trigonometric, it is possible to found a direct relation between the active machining force \vec{F}_a and the shear angle Φ . First the relation between active machining force \vec{F}_a and the chip normal force $F_{\Phi n}$ is determined by the Equation 6.

$$|\vec{F}_a| = \frac{|\vec{F}_{\Phi}|}{\cos(\xi)} \quad (6)$$

Figure 8 – THALES circle.



Source: Author.

Defined this force relation, it is necessary to express it in function of the shear angle Φ , the rake angle γ_o and β . Using sum of triangle internal angles, it is easy to see that $\xi = \Phi + \beta - \gamma_o$. Joining this relation with the Equation 5, an alternative expression for the active force \vec{F}_a can be written as shown in Equation 7. As required \vec{F}_a is function of Φ , β and γ_o and shear angle Φ is obtained, as shown by Equation 7.

$$|\vec{F}_a| = \frac{\tau_\Phi}{\sin(\Phi)} \frac{bh}{\cos(\Phi + \beta - \gamma_o)} \quad (7)$$

2.3.3 Shear angle determination

In order to determine the shear angle Φ in function of the rake angle and friction coefficient μ , Merchant (1945b) propose an approach based on an energetic analysis. The chip formation behavior is assumed to seek for a minimum level of energy, allowing to determinate the shear angle Φ by differentiating the power of the cutting process. Assuming the cutting force \vec{F}_c is the main responsible for the machine power consumption P , the Equation 8 can be written. The criterion of minimum energy in function of Φ is then applied, as shown in Equation 9 and in Equation 10.

$$P = \vec{F}_c \cdot \vec{v}_c = |\vec{F}_c| |\vec{v}_c| \cos(0^\circ) \quad (8)$$

$$\frac{\partial P}{\partial \Phi} = \frac{\partial |\vec{F}_c| |\vec{v}_c|}{\partial \Phi} = |\vec{v}_c| \frac{\partial |\vec{F}_c|}{\partial \Phi} = 0 \quad (9)$$

$$\frac{\partial^2 P}{\partial \Phi^2} = |\vec{v}_c| \frac{\partial^2 |\vec{F}_c|}{\partial \Phi^2} \neq 0 \quad (10)$$

Established the relation between the active force \vec{F}_a with the shear angle Φ , it is easy to relate this angle with the cutting force \vec{F}_c , using the Figure 8, as shown by the Equation 11.

$$|\vec{F}_c| = |\vec{F}_a| \cos(\gamma_o - \beta) = \tau_\Phi b h \frac{\cos(\gamma_o - \beta)}{\sin(\Phi) \cos(\Phi + \beta - \gamma_o)} \quad (11)$$

Joining the Equations 9 and 11 and using the condition of Equation 10 the Equation 12 it is found, determining the shear angle Φ .

$$\Phi(\gamma_o, \beta(\mu)) = 45^\circ + \frac{\gamma_o - \beta}{2} \quad (12)$$

The experimental verification of shear angle Φ value were performed by few authors. The results obtained by Zvorykin (1893) diverges from the the Equation 12, indeed, it obey the empirical law expressed by Equation 13, where the Zvorykin constants A_1 and A_2 are experimentally determined.

$$\Phi(A_1, A_2) = A_1 + A_2(\gamma_o - \beta) \quad (13)$$

Numerical investigations performed by Bäker (2005) and Garrido et al. (2006) also points to a divergent value of shear angle Φ than the obtained analytically by energy minimization criterion. In order to found a better analytical model for the shear angle determination, Molinari e Moufki (2008) approached the orthogonal cutting theory considering also the stability criterion of the chip morphology, providing this way the Equation 14 to determine the shear angle Φ . The model introduces a new variable θ , which is the chip inclination angle.

$$\Phi(\gamma_o, \beta(\mu), \theta) = 45^\circ + \frac{\gamma_o - \beta - \theta}{2} \quad (14)$$

These two alternative formulations for the shear angle Φ tends to converge to a value closer to experimental results, as show by Molinari e Moufki (2008).

2.4 Kienzle force model

The prediction of machining forces is a powerful tool to determine the power employed by a machining tool in the cutting process, moreover its prediction can be used applied at the orthogonal cutting theory and hence at Merchant's model. Series of machining tests following up the machining forces, such as performed by Lalwani, Mehta e Jain (2008), verified an empirical direct relation between the cutting force \vec{F}_c , the uncut chip width b and thickness h . Before this and many finds on literature, Kienzle (1952) had already developed a formulation relating these parameters, as present in Equation 15. The influence of the machined material, process, and tool geometry is given by the specific cutting pressure K_s .

$$|\vec{F}_c| = K_s b h \quad (15)$$

The specific cutting pressure K_s is also dependent of the uncut chip area A_{ch} , being inversely proportional to the chip thickness h , as described by the Equation 16, where $k_{s,1}$ is the specific cutting pressure for uncut chip thickness h equals to 1mm, and z is the force gradient, these two constants are the Kienzle's constants.

$$K_s = k_{s,1} h^{-z} \quad (16)$$

Joining the Equations 15 and 16 the cutting force \vec{F}_c assumes the format of Equation 17.

$$|\vec{F}_c| = k_{s,1} b h^{(1-z)} \quad (17)$$

To relate the cutting force directly with the cutting parameters f and a_p , the Equation 17 must consider the cutting edge angle κ_r , assuming the format of the Equation 18.

$$|\vec{F}_c| = k_{s,1} a_p (f \sin(\kappa_r))^{(1-z)} \quad (18)$$

The specific cutting pressure K_s dependence of the uncut chip thickness h it is easier visualized by manipulation of the Equation 17, linearizing it. This linearization also allows an easy determination of the Kienzle's constants experimentally, by measuring the cutting force and relating the uncut chip dimensions with the cutting parameters. The manipulation is shown in the Equation 19. This equation is used for the experimental purpose of this work, as detailed in Results.

$$\frac{|\vec{F}_c|}{b} = k_{s,1} h^{(1-z)} \implies \log \frac{|\vec{F}_c|}{b} = \log k_{s,1} + (1-z) \log h \quad (19)$$

The Kienzle's model it is also valid to determine the feed force \vec{F}_f but instead the use of specific cutting pressure $k_{s,1}$, the constant used must be the $k_{f,1}$ which is the specific cutting pressure in the feed direction for a uncut chip thickness h equals to 1mm, and a new gradient x takes place instead the z variable.

3 EXPERIMENTAL APPROACH

Based on the models to study the cutting force and cutting parameters, an experimental study is proposed. The goal of this study is to determinate experimentally the value of the cutting and feed forces in an orthogonal cutting process, and hence the shear angle Φ and the Kienzels constants.

To perform this work the machining process of shaping was chose, once it approaches an ideal orthogonal cutting, besides the facility of force measurement provided by it, when compared to others (e.g, turning, face milling, drilling, etc.).

In order to measure the active forces in the process, a new tool holder for a shaping machine was developed. This tool holder was designed aiming to be instrumented with deformation sensors (strain gauges), and be able to attach different cutting tools.

3.1 Tool holder design

To a successful force measurement, the design of the tool holder must accomplish the following boundary conditions:

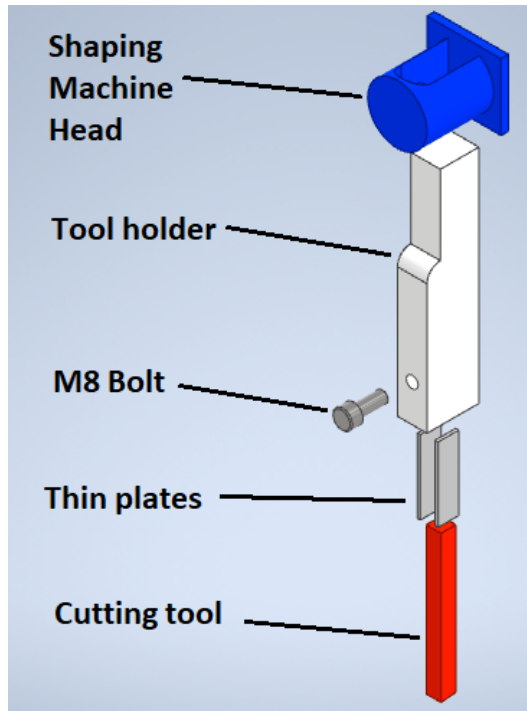
- Be able to be attached to the shaping machine used in this work;
- Be able to attach strain gauge sensors, i.e to have a region with uniform stress;
- Be able to attach different cutting tools;

Based on this boundary conditions, a simple geometry for the tool holder was developed. The first design requirement was accomplished based on the dimensions for clamp the tool holder in the shaping machine used in this work.

The second requirement was accomplished adopting a simple geometry (rectangular cross sections), in order to obtain surfaces with a constant stress distribution and hence allowing the placement of strain gauges. The third requirement was relatively hard to be accomplished: The tools available for this work has a square cross section, this way the holder body was designed with a square hole to attach the the tools. The challenge behind this requirement was the square format of the hole. However it could be done using drilling processes aligned with a file processes.

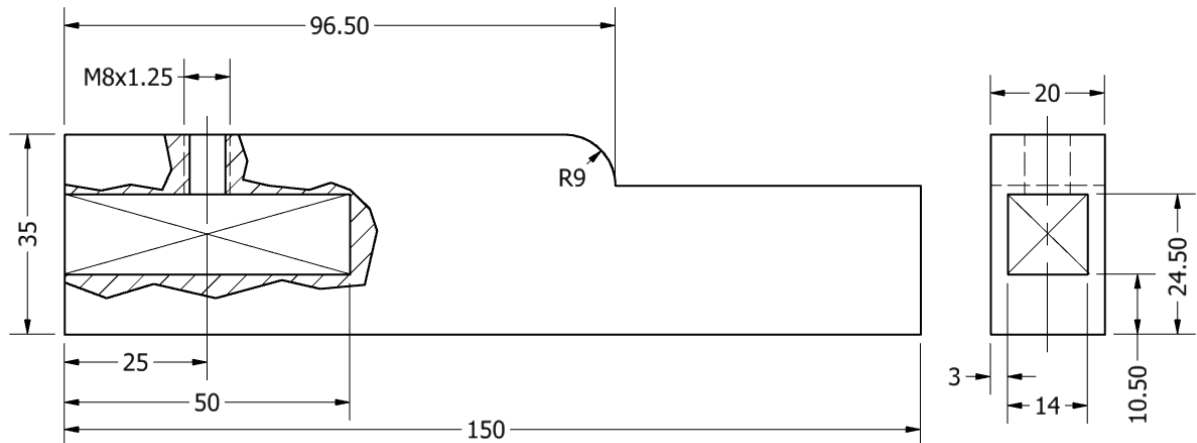
To fix the cutting tool in the tool holder, a M8 bolt is used, together with two steel thin plates. The tool holder is made by H13 hardened steel. The Figure 9 shows an exploded view of the cutting assembly, the Figure 10 a graphic representation of the tool holder design and the Figure 11 shows the final version of the tool holder, already assembled in the experimental setup.

Figure 9 – Exploded view of the cutting setup assembly.



Source: Author.

Figure 10 – Graphic representation of the tool holder design.



Source: Author.

3.2 Force measurement

Force measurement can be done by different ways, using different types of sensors. The most common are the dynamometer, piezoelectric sensor, and strain gauge. Each sensor works by different ways and has its advantages for different applications.

The force measurement present in this study is made using a strain gauge, which measures force by an indirect way, i.e., the sensor does not measure the force, but instead it measures deformation. The working of a strain gauge and its setup is discussed in 3.2.2. In

Figure 11 – Tool holder in the experimental setup.



order to determinate the force is necessary to convert the deformation measured into a stress and then convert this stress to a force.

The conversion between these quantities requires use of materials mechanics, relating to the Hooke's Law. A discussion about the use of this law is present below, in 3.2.1. Finally, the analytical model of the process used to correctly determinate the active cutting force \vec{F}_a is presented in 3.2.3.

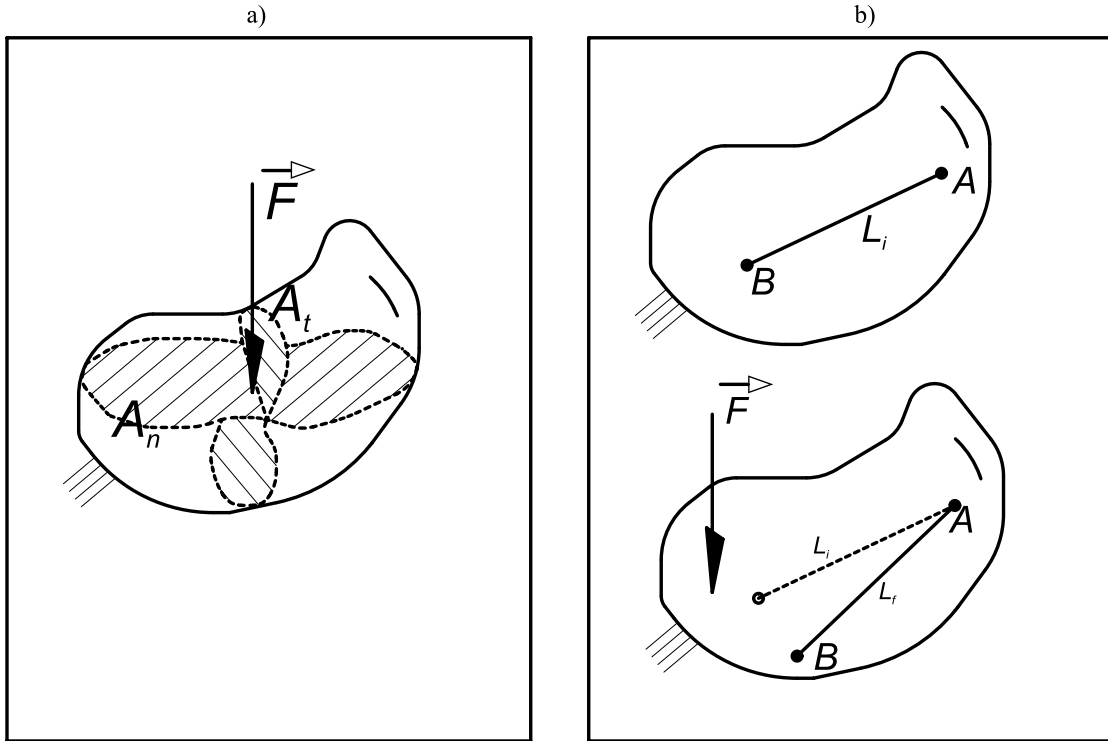
3.2.1 Force, stress and strain

When a non-rigid body, with no degrees of freedom, is subject to a force, the body suffers a deformation, it means, its geometry changes while the body is subjected to the force. If the force is big enough, the body remains deformed forever, even if the force stops (BEER et al., 2014).

This deformation is related to the stress made by a force. There are two types of stress created by a force \vec{F} applied to an area A : The normal stress, $\vec{\sigma}$, and the average shear stress, $\vec{\tau}$. The normal stress happens to an area A_n perpendicular to the force direction, and the average shear stress happens to an area A_t parallel to the force direction, as shown by the Figure 12a. A mathematical relation between the applied force, the areas and the resultant stresses for simple cases, is present in Equations 20 and 21.

$$\vec{\sigma} = \frac{\vec{F}}{A_n} \quad (20)$$

Figure 12 – Visualization of stress and strain in a body: a) Force being applied to a perpendicular and a parallel area; b) Relative displacement while a force is applied to a body.



Source: Author.

$$\vec{\tau} = \frac{\vec{F}}{A_t} \quad (21)$$

Both types of stress cause the relative displacement of points in the interior of the body, as shown in Figure 12b. Before the force application the point B was at a distance L_i from the point A. When the force is applied the point, B acquires a new distance L_f from point A. This relative displacement can be normalized as a normal strain ϵ , as shown by the Equation 22.

$$\epsilon = \frac{L_f - L_i}{L_i} \quad (22)$$

A first relation between stress and strain is given by the Hooke's law, shown in the Equation 23. The elastic modulus E is usually obtained by an uniaxial tensile test.

$$\sigma = E\epsilon \quad (23)$$

It is important to note that the stress at a point depends on the analysis direction, it means, if the reference frame where the analysis is being made rotates, the stress values, of the point, in the new reference frame will be different. The same occurs for strains. Due to this, the Equation 23 can only be used for an uniaxial state stress using the correct

framework, where the only stress present is the normal (BEER et al., 2014). In other cases, where there are other stresses, the relation between stress and strain consider three orthogonal directions of analysis and must use the general Hooke's law, present in the Equations 29, 30 and 31.

Besides the normal strain, the body also suffers another strain: the shear strain γ . The shear strain γ is related with the average shear stress τ by the Equation 24. The shear modulus G is related to the elasticity modulus by the Equation 25. The Poisson's ratio ν in this equation is given by the ratio between strain ϵ_y in a perpendicular direction of the stress and the strain ϵ_x in the stress direction, as shown by Equation 26.

$$\tau = G\gamma \quad (24)$$

$$G = \frac{E}{2(1 + \nu)} \quad (25)$$

$$\nu = -\frac{\epsilon_y}{\epsilon_x} \quad (26)$$

As mentioned, if the reference frame changes, the stresses and the strains in a point also changes. At Figure 13 an infinitesimal point under two normal stresses, σ_z and σ_y , and to shear stress τ_{zy} , is being rotate by an angle θ in counter-clockwise direction. At the new frame, the normal stresses are now σ'_z and σ'_y and the shear stress became τ'_{zy} . The relations between these stresses in both frames are presented by the Equation 27 and between the strains (the ones occurring at same directions of these stresses), by the Equation 28.

$$\begin{aligned} \sigma'_z &= \frac{\sigma_z + \sigma_y}{2} \pm \frac{\sigma_z - \sigma_y}{2} \cos(2\theta) \pm \tau_{yz} \sin(2\theta) \\ \sigma'_y & \end{aligned} \quad (27)$$

$$\begin{aligned} \epsilon'_z &= \frac{\epsilon_z + \epsilon_y}{2} \pm \frac{\epsilon_z - \epsilon_y}{2} \cos(2\theta) \pm \frac{\gamma_{yz}}{2} \sin(2\theta) \\ \epsilon'_y & \end{aligned} \quad (28)$$

Well-established the definition of stress and strain, its rotations and the elastic constants, the general Hooke's law is present in the Equations 29, 30 and 31, relating the stress and strain in three orthogonal directions.

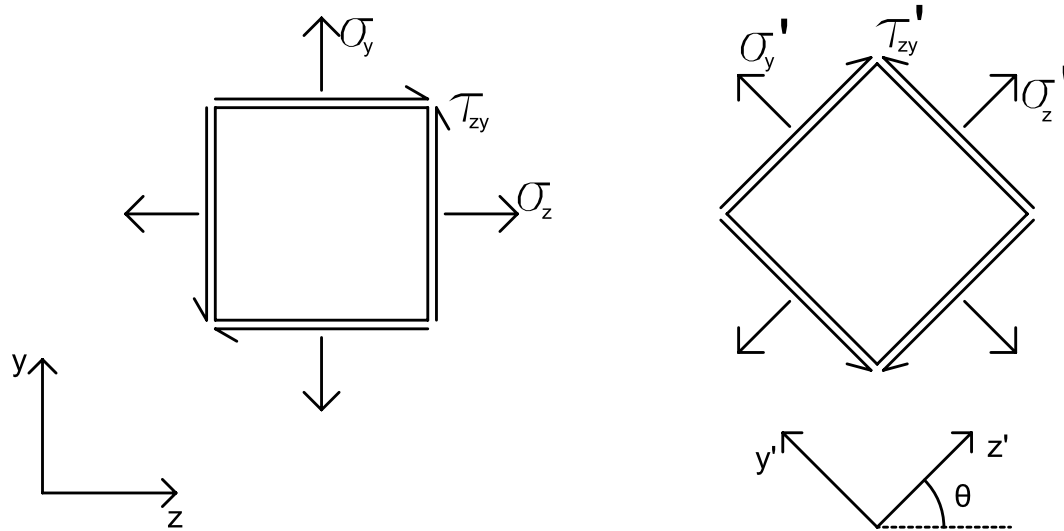
$$\epsilon_x = \frac{\sigma_x - \nu(\sigma_y + \sigma_z)}{E} \quad (29)$$

$$\epsilon_y = \frac{\sigma_y - \nu(\sigma_x + \sigma_z)}{E} \quad (30)$$

$$\epsilon_z = \frac{\sigma_z - \nu(\sigma_y + \sigma_x)}{E} \quad (31)$$

A few considerations must be made about the Hooke's general law: It only can be applied until the stress in the body does not deform it plastically (which means when

Figure 13 – Rotation of reference frame in a point under normal and shear stress. Rotation of θ rad in the anti clockwise direction.



Source: Author.

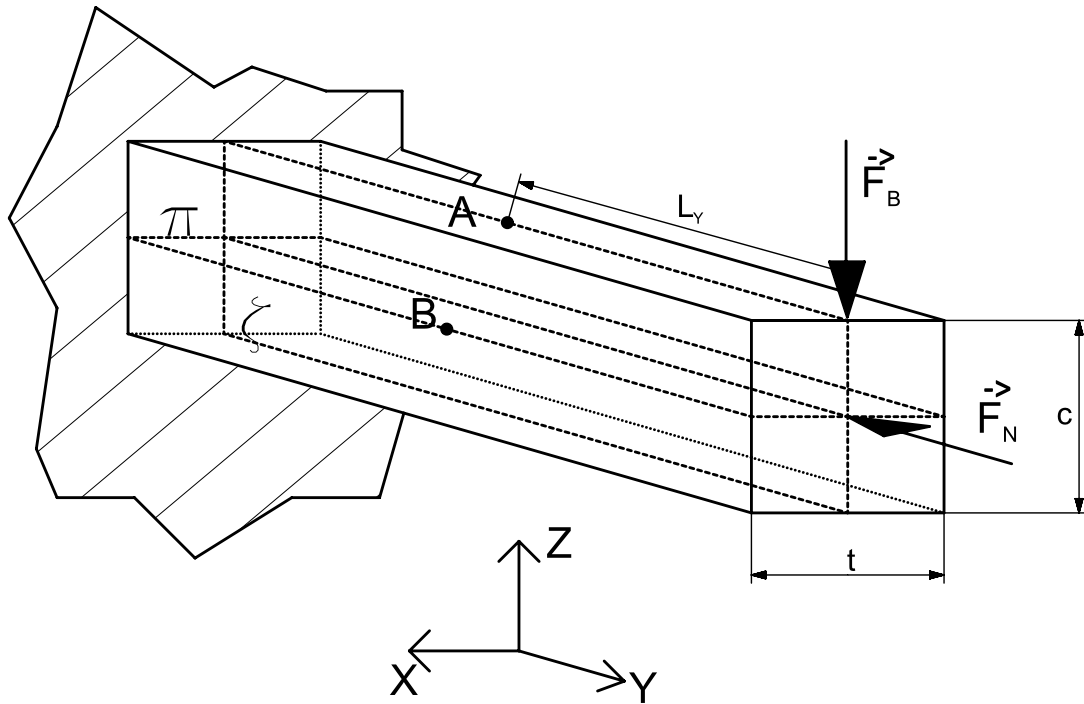
the stress ends, the body returns to its original shape), and is just valid for bodies with an isotropic configuration (Their mechanical properties are the same for every direction).

In general cases the relation between force and stress is not simple as the equation 20 and 21, due to the geometry of the body. For this work, the relation of stresses and forces at two points of a cantilever beam, with a rectangular cross section, under a compression force \vec{F}_N and a bending force \vec{F}_B , is used. The Figure 14 shows a cantilever beam with these loads. The points of analysis are the point A and B. The reason for choosing these points is due to the location of the strain gauges, more details are present in 3.2.3.

At Figure 14 the points A and B are both located at a distance L_Y from the face where the forces are being applied. The planes π and ζ cut in half the beam, and are parallel to the planes XY and ZY, respectively. The point A is on the beam surface parallel to the π plane and is also contained in the ζ plane. The point B belongs to π plane and is contained in the beam surface parallel to the ζ plane. The beam has a thickness t and a width c .

A cantilever beam contains in its center the called neutral axis, a line where there is no normal stress caused by bending forces and maximum shear stress caused by it. For a first view, this monograph assumes that an axial load does not move the neutral axis. At Figure 14 the neutral axis is given by the intersection between the planes π and ζ . Due to that, the bending force \vec{F}_B , causes a normal stress σ_A in Y direction, on point A and a shear stress τ_B in Z direction, on point B. The normal stress for this configuration is given

Figure 14 – Cantilever beam under a bending force and a compression force.



Source: Author.

by the Equation 32, and the shear stress by the Equation 33. The normal force, \vec{F}_N , only causes normal stress, and for both points A and B this stress is given by the Equation 20.

$$\sigma_A = \frac{M d_A}{I} = \frac{(F_B \cdot L_Y) \frac{c}{2}}{I} \quad (32)$$

$$\tau_B = \frac{3 F_B}{2 A_c} = \frac{3 F_B}{2 t \cdot c} \quad (33)$$

In the Equations 32 and 33 the variables M , d_A , I , and A_c are respectively the total moment acting in the neutral axis caused by the forces (Note that the normal force F_n does not cause moment because are contained in the neutral axis, otherwise it must be considered), the distance from point A to neutral axis, moment of inertia of the cross section (for a rectangular cross section $I = ((width) \cdot (height))^3 / 12$) and the area of the cross section. Combining the Equations 32 and 20 the Equation for the total normal stress σ^A in the Y direction on point A is obtained, as shows by Equation 34. Since the normal force \vec{F}_N does not causes shear stress in direction Z on the point B (assuming the length of the cantilever is much bigger than it other dimensions), the total shear stress in this point it is already given by the Equation 33.

$$\sigma^A = \frac{Md_A}{I} - \frac{F_n}{A_c} = \frac{(F_B \cdot L_Y) \frac{c}{2}}{I} - \frac{F_n}{t \cdot c} \quad (34)$$

3.2.2 Strain gauge

Strain gauges are sensors which measure deformation based on Ohm's law. A strain gauge works as an resistor with variable resistance, its resistance varies in function of its length, and hence, in function of its deformation. As its resistance R varies, the voltage U also varies, as described by the first Ohm's law, showed in the Equation 35, where i is the current passing through the resistor.

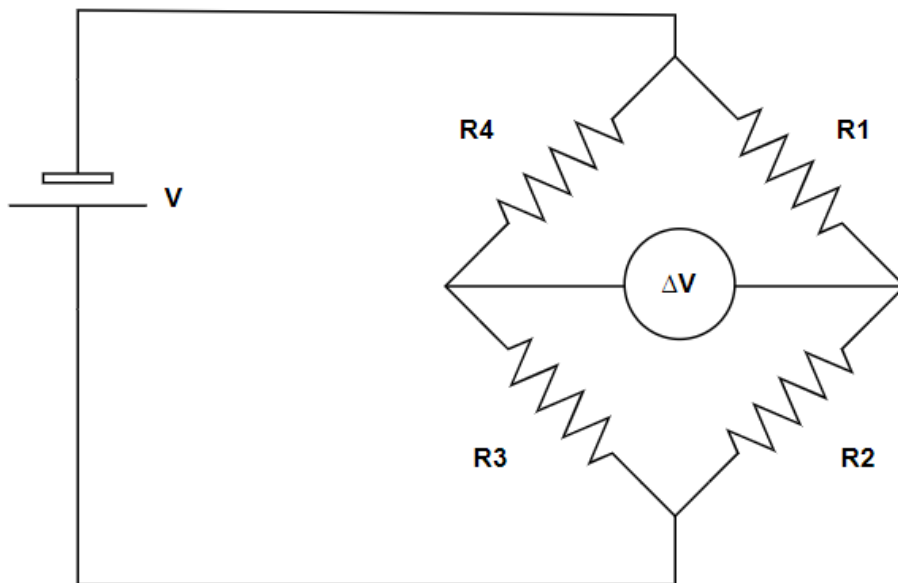
$$U = Ri \quad (35)$$

The resistance dependence with the resistor length L_r is given by Equation 36, where A_r is the area of resistor cross section and ρ is its resistivity. For strain gauges this resistivity is considered constant in its range of work.

$$R = \frac{\rho L_r}{A_r} \quad (36)$$

Using both Ohm's law it is possible to obtain the deformation of a strain gauge measuring its voltage. To amplify this voltage read, the strain gauges are usually assembled in a Wheatstone bridge circuit. An example of this circuit is shown by the Figure 15. This circuit is being supplied by a voltage V .

Figure 15 – Wheatstone bridge circuit.



Source: Author.

Table 1 – Strain Gauge 1-XY41-3/350 resistance and dimensions.

Nominal resistance Ω	Gauge factor	Maximum voltage supply [V]	a [mm]	b1 [mm]	b2 [mm]	c [mm]	d [mm]
350	2,05	9	3	4,2	5,6	11	8

When the product of the resistance R_1 by R_3 is equal to the product of R_2 by R_4 the circuit is considered in equilibrium, which means the voltage reading ΔV is equal to zero. If one of its resistance is replaced by a strain gauge, any deformation in it will cause the imbalance of the bridge, causing a voltage ΔV reading different than zero.

The relation between the voltage read ΔV and the variance of each resistance is given by the Equation 37 (HOFFMANN, 1989).

$$\Delta V = \frac{V}{4} \left(\frac{\Delta R_1}{R_1} + \frac{\Delta R_3}{R_3} - \frac{\Delta R_2}{R_2} - \frac{\Delta R_4}{R_4} \right) \quad (37)$$

Deriving the Equation 36 it is possible to obtain the relation $\Delta R/R$ for a strain gauge, relating it directly with the strain. The relation is given by Equation 38, where k is the gauge factor of the strain gauge, a constant value for each strain gauge.

$$\frac{\Delta R}{R} = k\epsilon \quad (38)$$

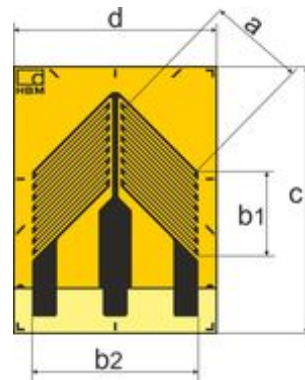
In this work all strain gauges used is assembled in a half bridge setup, which means two of four resistors are replaced by two strain gauges. The resistors replaced for the measurement are R_1 and R_2 . They are choose in order to avoid the influence of strains caused by thermal variations. Assuming the resistors R_3 and R_4 does not varies its resistance, and replacing the Equation 38 into Equation 37 a subtraction relation is obtained, as shown by the Equation 39, where ϵ_{R1} and ϵ_{R2} are the strain of each strain gauge.

$$\Delta V = \frac{Vk}{4} (\epsilon_{R1} - \epsilon_{R2}) \quad (39)$$

This relation of subtraction between the strains is very useful, once the strain gauge material is different than the tool holder material, which implies in different deformations due to temperature variation. Using this subtraction, the strain caused by temperature variation is eliminated. Besides it, this subtraction is used in the modelling of the process, as described in 3.2.3.

For this work, the strain gauges used are already assembled in pair contained in a grid. The model used in this work is the 1-XY41-3/350. It has a “V” setup with an angle of 90° between each strain gauge, as shown by Figure 16. Its data are shown in Table 1.

Figure 16 – Grid of strain Gauge 1-XY41-3/350.



Source: HBM.

3.2.3 Modelling with strain gauge

To relate the cutting forces with stresses and strains in the shaping process, using the general Hooke's law, an analytical model of the process is required. To define a good model, the running of the process need to be known in order to make good mathematical approximations.

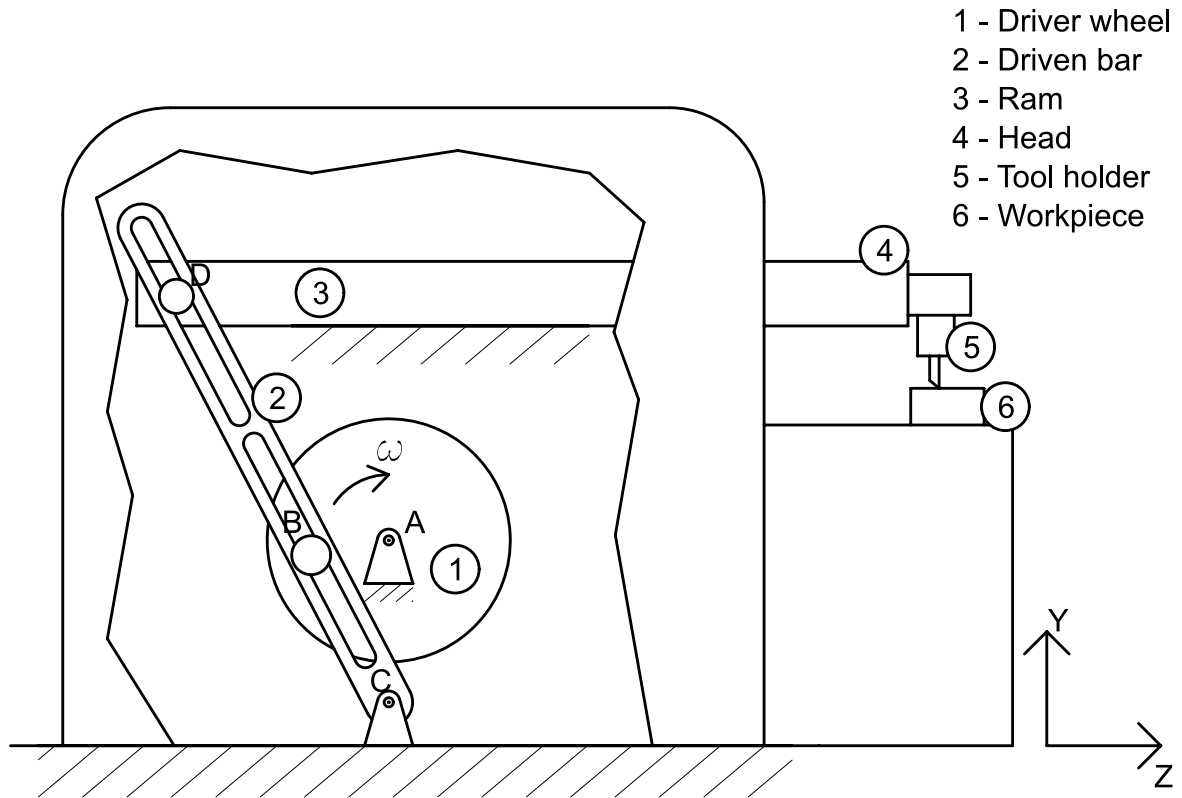
The kinematics behavior of the shaping process is shown in the Figure 17. The energy source for the cutting movement is provided by an electric motor attached to a gearbox. This gearbox is connected to a driver wheel (1) pivoted at the point A. This driver wheel contain a eccentrically pin (point B), which is inside a oblong hole in the driven bar (2). This driven bar is pivoted at point C, in way that the circular motion of the driver wheel causes an back and forth angular movement on the bar. A second oblong hole in the driven bar holds a pin attached to the ram (3) (point D). The ram has it movement restricted to the Z axis only, such way that the driven bar movement causes a linear back and forth movement of the ram. At the head of the ram (4) the tool holder is embedded, performing this way the cutting movement.

Due to this kinematics of the shaping process, even if the motor of the shaping machine is in a constant speed, the tool holder will realize a cutting in a non constant speed. However, if the length of cutting is big enough, the tool holder speed in the middle of the path can be approximate to constant. This is the first assumption for the appliance of the generals Hooke's law.

The Figure 18 shows the front view of the actual shaping machine used in this work. Note the machine dimensions, higher than the tool holder dimensions, and stiffer also. This difference in size (and hence mass), and stiffness allows treat the tool holder as a cantilever beam with a rectangular cross section.

Once the tool holder is approached as a cantilever beam, the place where the strain gauges are bonded and it directions will determinate the correct mathematical equations of the models.

Figure 17 – Schematic representation of the running system of a shaping machining. Points A,B,C,D indicates the link points between the machine elements. Dimensions and elements positions are merely illustrative.



Source: Author.

The idealized placement for strain gauges in the tool holder is shown in Figure 19. The orientation and the exactly place of each pair of strain gauge were designed based on the goal of reach the strain which will allow to obtain the normal stress on the back face of the tool holder and the shear stress on it lateral face. The relation between the strains measured by each pair and the stresses is discussed below, and the validation of the relation is presented in 3.2.4.

Considering the feed as the $Z+$ direction, and the vertical direction the Y axis, each strain gauge will be denominated by “SG_(FACEPLACED)(DIRECTION)”. Each face of the tool holder is named by the normal vector to it, e.g the back face is the $Z-$. When the notation does not count with the direction, it is referring to the pair of strain gauge of that face. The directions U and V are respectively the direction Z and Y rotated by 45° around the X axis, in the anti clockwise direction.

Considering SG_Z-Y and the SG_Z-X assembled in a half Wheatstone bridge, replacing respectively the resistors R_1 and R_4 , the Equation 39 becomes the Equation 40.

$$\Delta V = \frac{Vk}{4}(\epsilon_y - \epsilon_x) \quad (40)$$

Figure 18 – Actual shaping machine used in this work.



Source: Author.

If it is assumed a planar state of stress in the strain gauge location, with the stress in the X direction being zero ($\sigma_x = 0$) (which is verified in 3.2.4), the subtraction between the Equation 30 and 31 will result in the Equation 41

$$\epsilon_y - \epsilon_x = \frac{\sigma_y}{E}(1 + \nu) \quad (41)$$

Substituting the Equation 41 into Equation 40 the voltage signal read can be related directly with the stress σ_y in the strain gauge place, as shown in the Equation 42.

$$\Delta V = \frac{Vk}{4} \frac{\sigma_y}{E}(1 + \nu) \quad (42)$$

For the lateral face, considering SG_X-U and SG_Y-V also assembled in half bridge, replacing respectively the the resistors R_1 and R_2 , the Equation 39 becomes the Equation 43

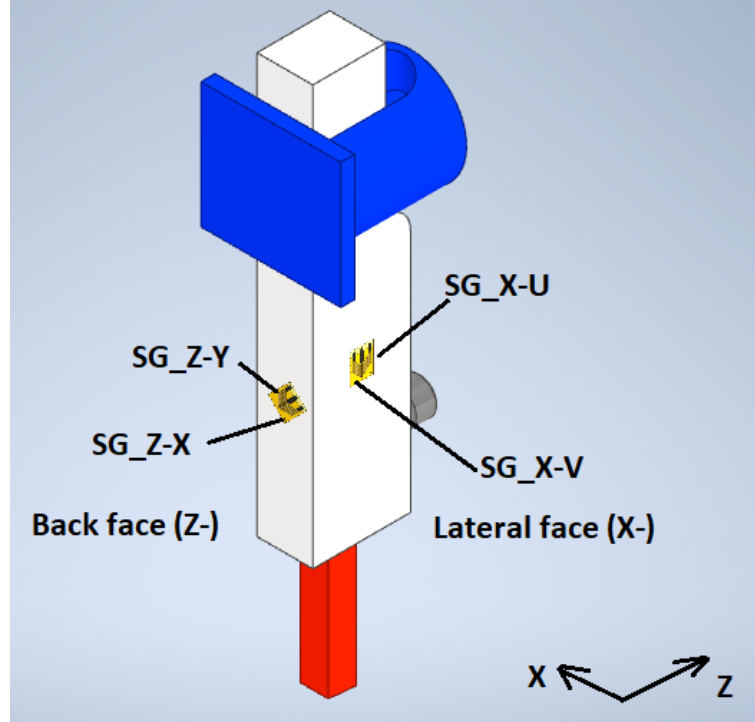
$$\Delta V = \frac{Vk}{4}(\epsilon_u - \epsilon_v) \quad (43)$$

Since the U and V directions the directions Z and Y rotated by 45° in anti clockwise direction, the equation 28 can be used to determinate the strain ϵ_u and ϵ_v . The resulting strain for each directions is shown in the Equation 44 and 45, respectively.

$$\epsilon_u = \frac{\epsilon_x + \epsilon_y}{2} + \frac{\gamma_{yz}}{2} \quad (44)$$

$$\epsilon_v = \frac{\epsilon_x + \epsilon_y}{2} - \frac{\gamma_{yz}}{2} \quad (45)$$

Figure 19 – Strain gauge placement on tool holder. In blue the tool holder support, in white the tool holder, in red the cutting tool and in grey the bolt for hold the tool.



Source: Author.

Subtracting the Equation 45 from Equation 44 a relation between the strain in directions U and V and the shear strain γ_{yz} is obtained, as shown by the Equation 46.

$$\epsilon_u - \epsilon_v = \gamma_{yz} \quad (46)$$

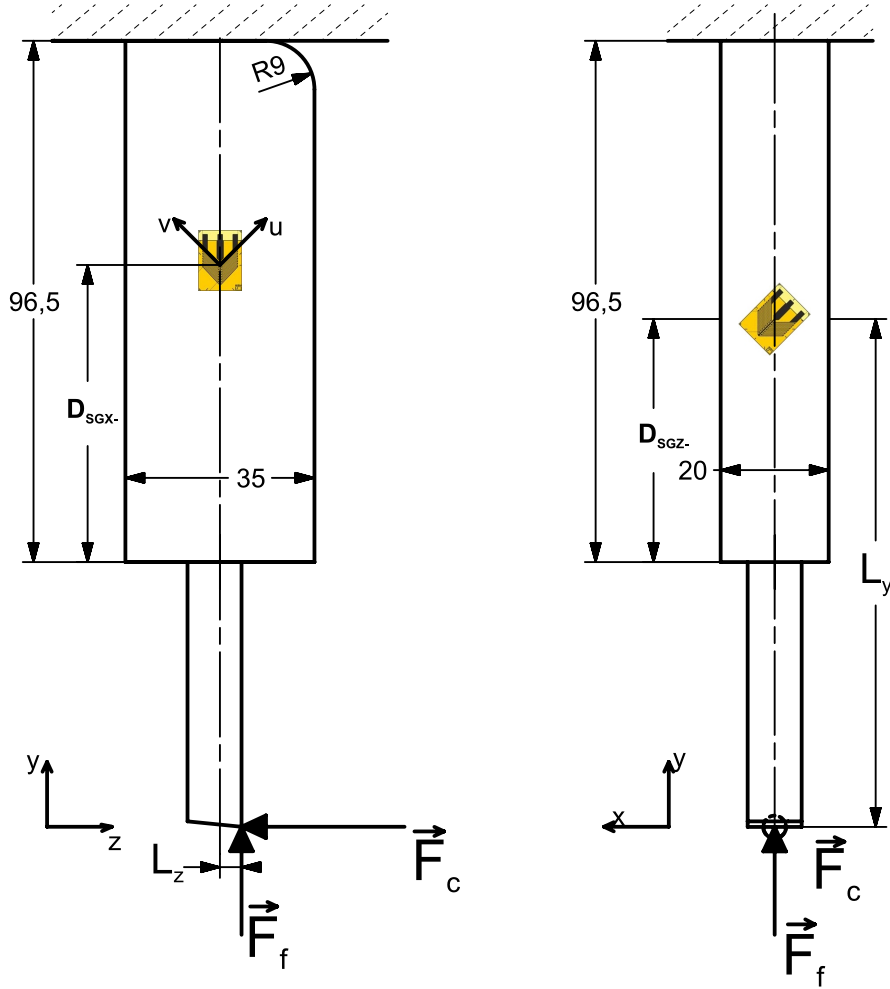
Considering the relation $\tau_{yz} = G\gamma_{yz}$ (From Equation 24) the voltage signal read can be related with the shear stress τ_{yz} in the strain gauge placed on the lateral face, as shown by Equation 47.

$$\Delta V = \frac{Vk}{4} \frac{\tau_{yz}}{G} \quad (47)$$

It is important to notice that the Equation 28 it is used for an infinitesimal point on a body, and the strain gauge actually read a large region. Due to this, a verification of the use of this modelling is present in 3.2.4.

Well established the relation between the stresses and the signal voltage read, it is possible to measure the cutting force and the feed using the cantilever beam model for the tool holder. The Figure 20 shows a free-body diagram of the tool holder, being approached as a cantilever beam. The relation between the stresses in the SG places, σ_{SG_Z-} and τ_{SG_X-} , is shown in the matrix Equation 48, adapted from Equations 33 and 34 with the tool holder dimensions.

Figure 20 – Tool holder free body diagram. Approached as a cantilever beam.



Source: Author.

$$\begin{bmatrix} \frac{-1}{20.35} + \frac{35/2}{20.35^3/12}L_z & -\frac{35/2}{20.35^3/12}L_y \\ 0 & \frac{3}{2} \frac{1}{20.35} \end{bmatrix} \begin{bmatrix} |\vec{F}_f| \\ |\vec{F}_c| \end{bmatrix} = \begin{bmatrix} \sigma_{SG_Z-} \\ \tau_{SG_X-} \end{bmatrix} \quad (48)$$

The distances L_y and L_z , on the free body diagram of the Figure 20 and in the Equation 48 are respectively the lever length between the cutting force \vec{F}_c and the SG_Z-, the distance between the feed force \vec{F}_f and the tool holder neutral axis. The distances D_{SG_X-} , and D_{SG_Z-} are the distance between SG_X- and SG_Z- between the bottom of the tool holder, respectively. These distances will be determinate based on the validation of the model using finite element method (FEM).

3.2.4 FEM validation

In order to validate the system modelling and to determinate the exact local for the strain gauges placement, a series of numerical simulations using the FEM technique

were performed.

The goal of the simulation is to use known forces as input to obtain the strain in the faces where the strain gauges are supposed to be stick. The strain obtained will be compared with the analytical strain obtained by combining the Equation 48 with the general Hooke's law. It is expected to found a region on the tool holder faces where both the analytical and numerical strains coincides, with a constant stress gradient. This region is the correct local for the strain gauge placement.

As described by Bathe (2008), the FEM technique consists in dividing the analysed body in discrete parts, called elements. Each part are connected to it neighborhood by nodes. Then the displacement, strain and stress of each element are determinated using the relation between it stiffness and the force suffered by it nodes. Details of the technique are not the scopes of this work, so it will not be deeper discussed.

The simulations were performed in the software NX12, using the solver NASTRAN. The CAD assembly used is shown by Figure 9. The Table 2 shows the parts used in the model and it elements sizes, nodes and elements numbers. The element used was the type tetrahedral with ten nodes each, the inputs in the simulation were the cutting and feed force, being applied in the cutting edge of the tool holder, the part "Support", representing the shaping machine head, was fully restricted in all degrees of freedom. All contacts between the parts were defined as bonded, due to the stiffness of the assembly.

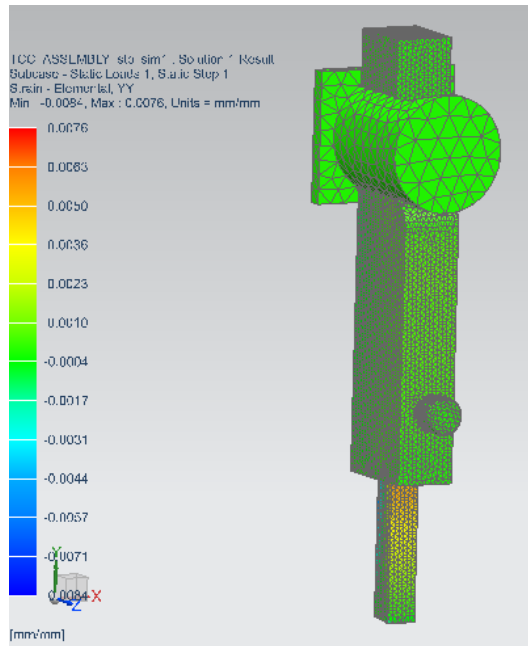
Table 2 – FEM Setup.

Part	Element Size [mm]	Number of elements	Number of nodes
Tool holder	2,00	112220	161670
Neutral cutting tool	2,00	13176	20175
Plate 1	2,00	2047	3796
Plate 2	2,00	2051	3802
Bolt	2,59	5938	9166
Support	10,00	1735	3334

Six sets of simulations were performed, being divided in three groups: The first group had simulation considering the ratio 5:2 between the cutting and feed force, the second group considerate the feed force as 65% of the cutting force. The first group simulation had as input the following pair of forces (Cutting force, Feed force): (500N, 200N); (1000N, 400N) and (5000N, 2000N), the second group counted with the following pair of forces: (500N, 325N); (1000N, 650N) and (5000N, 3250N).

As expected, due to the linear relationship between force and strain, as demonstrate in 3.2.1, the strain obtained using pair of forces following a same ratio presents strains following a linearity in each group. Once established this linearity between the results, this monograph will present only the results from the simulation using the pair of forces (5000N, 2000N) and (5000N, 3250N). The Figure 21 shows the mesh and the results for strain in the Y direction caused by the pair (5000N, 3250N).

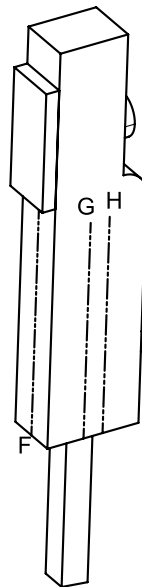
Figure 21 – Mesh and results for the pair of force (5000N, 3250N).



Source: Author.

To determine the distance SG-Z- the stresses and strains along the central line of the back face (Z-) were plotted in function of the distance from the bottom of the tool holder. The Figure 22 is a diagram of the query curves used to realize the plots.

Figure 22 – Query curves F,G,H used for the analysis.

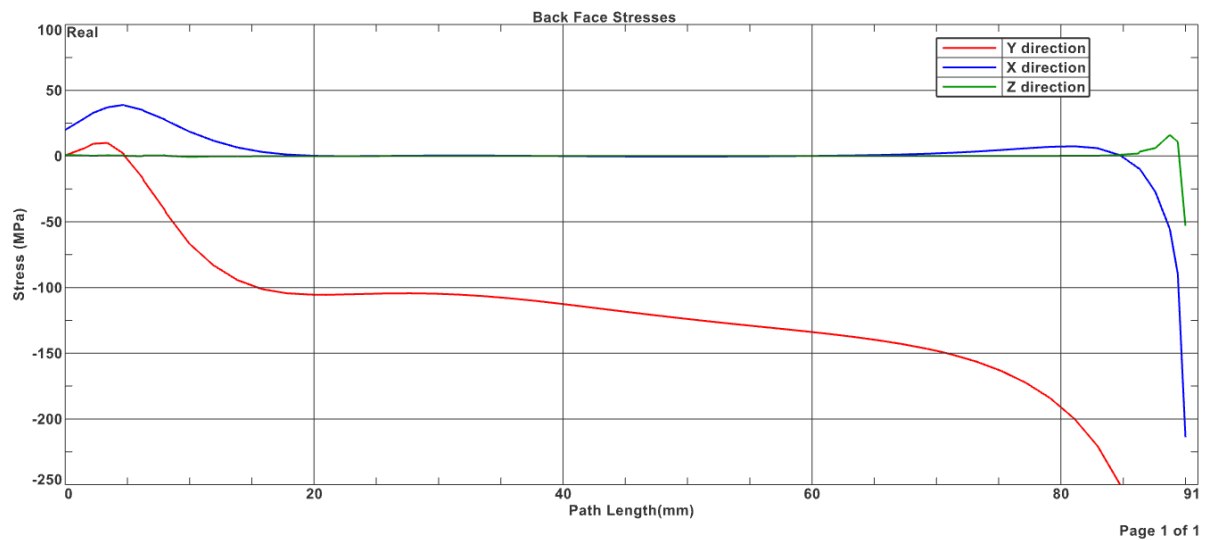


Source: Author.

The first variables analysed were the stresses in the back face. This analysis intend to compare the values between the normal stresses in the directions X, Y and Z, to assure

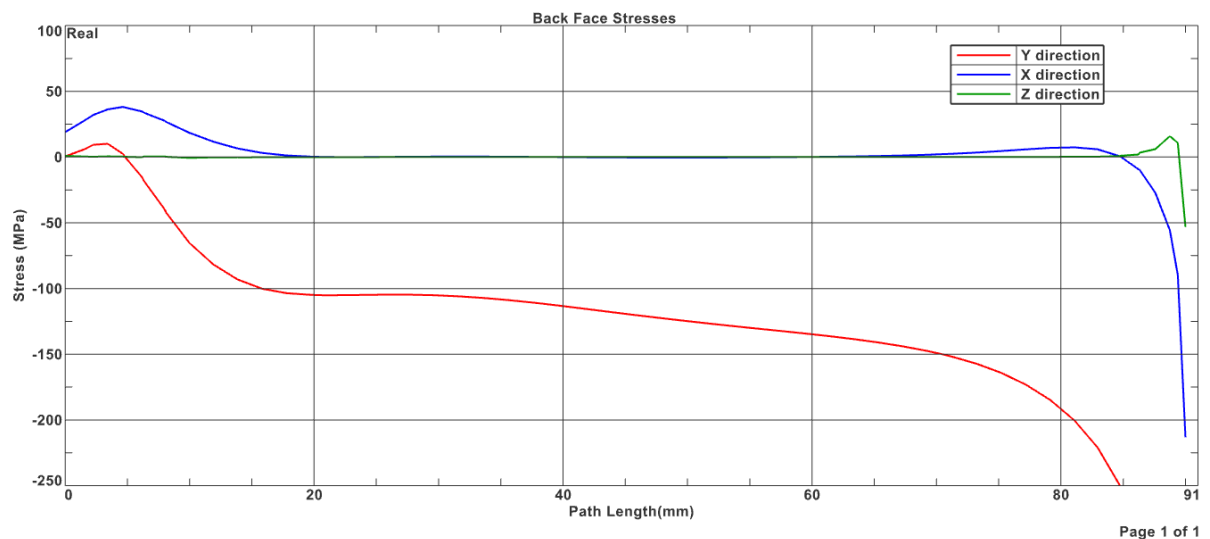
that the hypotheses of a planar state of stress is valid, and hence validate the equations used in the model. The Figures 23 and 24 shows the stresses in the three directions along the back face for the pair of forces of (5000N,2000N) and (5000N,3250N) respectively.

Figure 23 – Stresses along the back face of tool holder, using a cutting force of 5000N and a feed force of 2000N. The X axis contains the points located in the line F from the Figure 22.



Source: Author.

Figure 24 – Stresses along the back face of tool holder, using a cutting force of 5000N and a feed force of 3250N. The X axis contains the points located in the line F from the Figure 22.

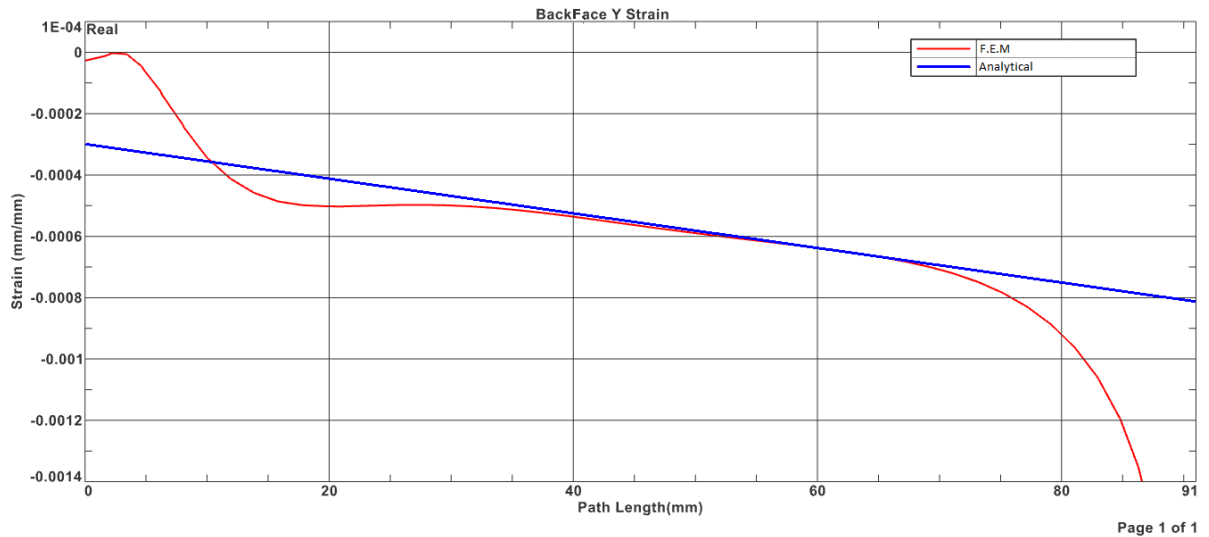


Source: Author.

The graphs in the Figures 23 and 24 point to a unidimensional state of stress in the back face of the tool holder, in the region between 20mm and 70mm from the tool holder bottom, validating the model's assumption of $\sigma_x = 0$. The validation of the

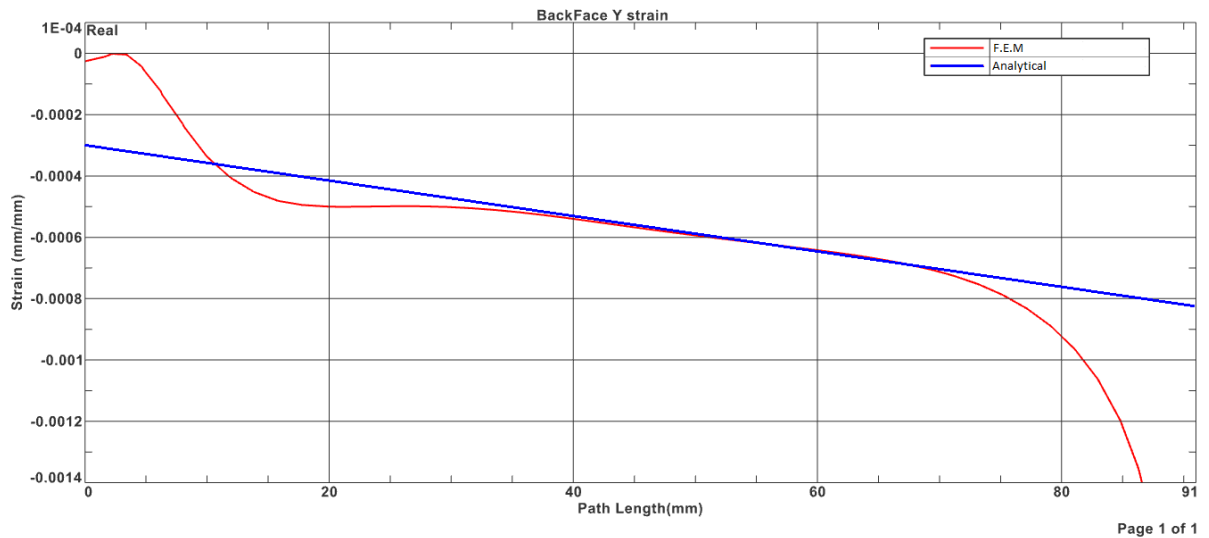
Equation 48 also was performed, the Figures 25 and 26 shows the results. Beyond the verification, the results were used to determinate the specific location to place the strain gauges.

Figure 25 – Strain in the Y direction along the back face of tool holder, using a cutting force of 5000N and a feed force of 2000N. The X axis contains the points located in the line F from the Figure 22.



Source: Author.

Figure 26 – Strain in the Y direction along the back face of tool holder, using a cutting force of 5000N and a feed force of 3250N. The X axis contains the points located in the line F from the Figure 22.



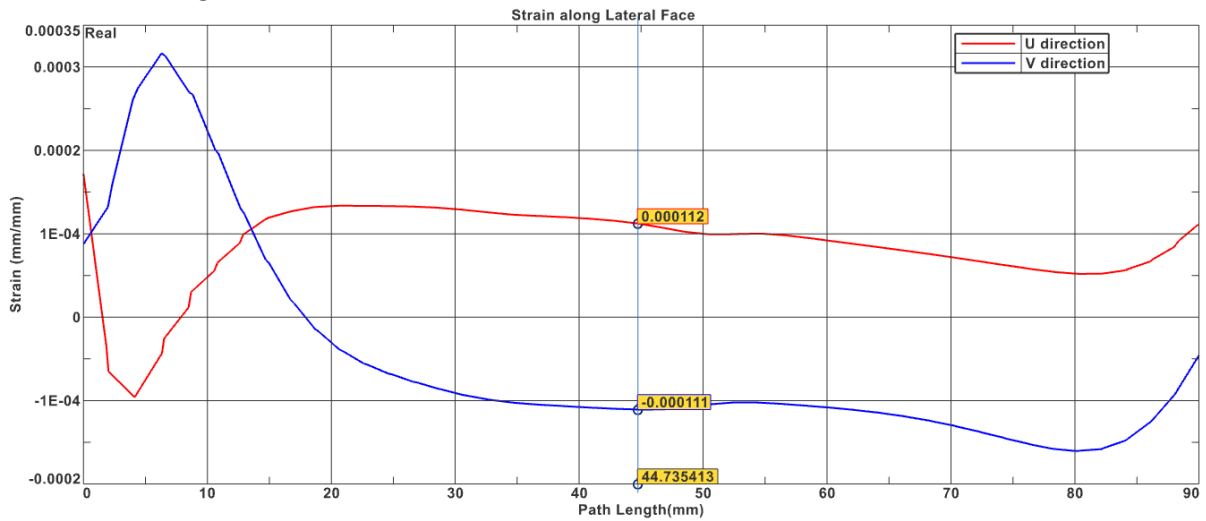
Source: Author.

The Figures 25 and 26 points to a convergence between the numerical results and the analytical results in the region between 40mm and 60mm from the tool holder

bottom. Due to this, the distance of 45mm from the bottom was chosen as local of gluing the center of SG_Z-.

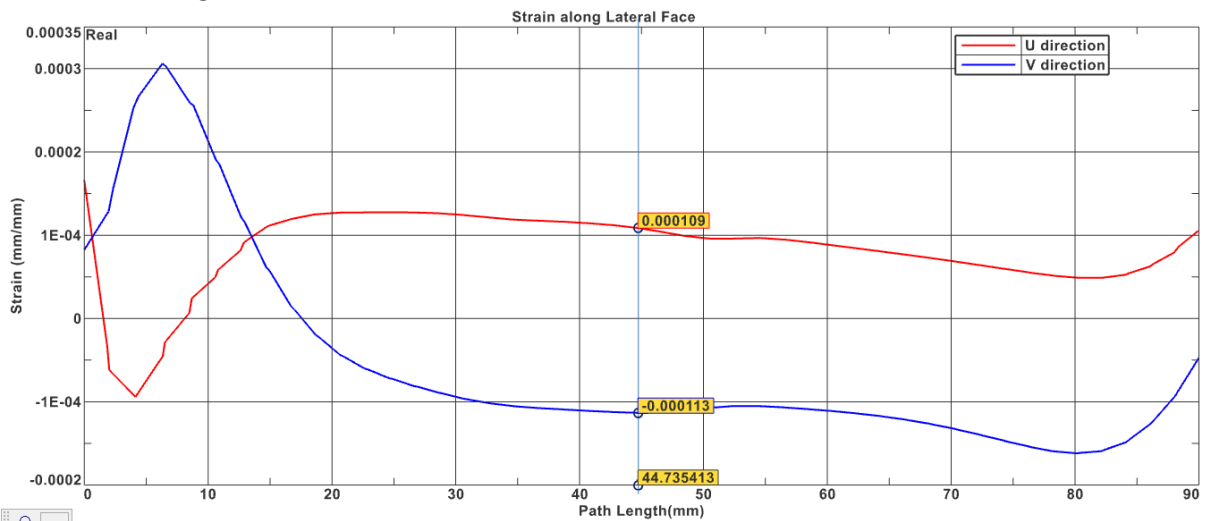
To determine the local of gluing for the SG_X-, the strain in the directions U and V were obtained using the line H, for U direction, and line G for V direction. The results are shown in the Figures 27 and 28.

Figure 27 – Strain in the U and V direction along the lateral face of tool holder, using a cutting force of 5000N and a feed force of 2000N. The X axis contains the distance to the bottom from the points located in the lines G and H from the Figure 22.



Source: Author.

Figure 28 – Strain in the U and V direction along the lateral face of tool holder, using a cutting force of 5000N and a feed force of 3250N. The X axis contains the distance to the bottom from the points located in the lines G and H from the Figure 22.



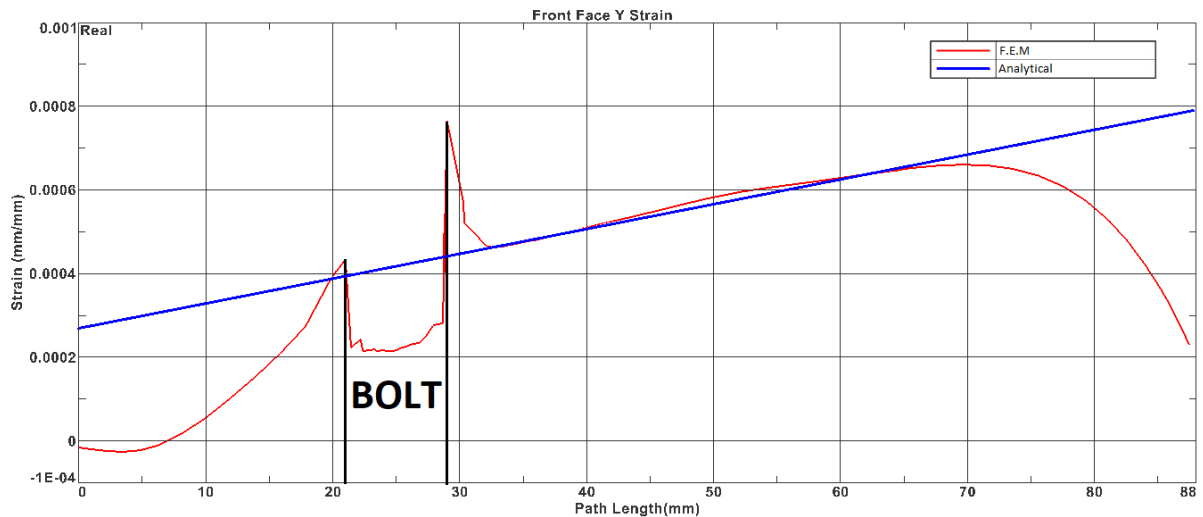
Source: Author.

From Equations 48 and 46 it is expected a difference between the strain in the U direction and V direction with absolute value of $1,65e-4$ for both pair of forces (5000N,2000N) and (5000N,3250N), since theoretically the feed force \vec{F}_f does not influence the shear strain. However, from the Figures 27 and 28, the difference between the strains, in the region of 45mm from the bottom of the tool holder, it is equal to $2,22e-4$ for the pair (5000N,3250N) and $2,23e-4$ for the pair (5000N,2000N), diverging around 70% from the value expected.

Perhaps the difference between the numerical value and the expected value is due to the displacement of the neutral axis, which is not considered in the analytical model. The displacement of the neutral axis is caused by the combination of a bending force with a compression force, and for different ratios between these forces, there are different neutral axis displacements.

This way, in order to avoid complications in the data acquisition, a pair of strain gauge with a similar disposition of the SG-Z- were chosen to be bonded in the front face of the tool holder, its notation is hence SG-Z+. A check of convergence in the tool holder front face between analytical strain and numerical strain was also performed, as shown by the Figures 29 and 30.

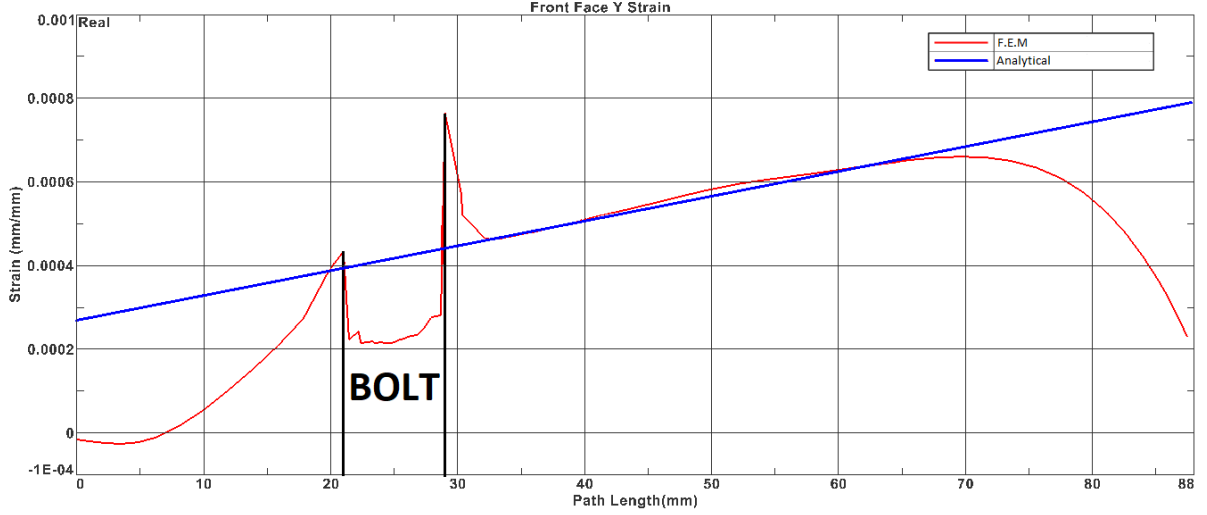
Figure 29 – Strain in the Y direction along the front face of tool holder, using a cutting force of 5000N and a feed force of 2000N. The X axis contains the points located in a line parallel to F line from the Figure 22, but located in the front face from the tool holder.



Source: Author.

As shown by the Figures 29 and 30, the distance of 45mm, from the bottom of the tool holder, presents a convergence between the analytical strain value and the numerical strain value. This way, the new strain gauge were stuck in this position. Note that in all simulations the strain non linearity occurred in the regions close to the tool holder bottom, is due to the abrupt change in inertia moment, due to the change in cross

Figure 30 – Strain in the Y direction along the front face of tool holder, using a cutting force of 5000N and a feed force of 3250N. The X axis contains the points located in a line parallel to F line from the Figure 22, but located in the front face from the tool holder.



Source: Author.

section.

A highlight must be made regarding the model of the process: It does not change with this alteration, however the second line of the matrix Equation 48 must be change, since we are not working with the shear strain anymore, it must be replaced with the equation for the strain in the Y direction from the front face. The Equation 34 allows the relation between this strain and the active machining forces, considering the signal of the neutral axis localization. Substituting the second line of the Equation 48 with the Equation 34, for the Y strain in the front face, the Equation 49 is then obtained.

$$\begin{bmatrix} \frac{-1}{20.35} + \frac{35/2}{20.35^3/12} L_Z & -\frac{35/2}{20.35^3/12} L_Y \\ \frac{-1}{20.35} - \frac{35/2}{20.35^3/12} L_Z & \frac{35/2}{20.35^3/12} L_Y \end{bmatrix} \begin{bmatrix} |\vec{F}_f| \\ |\vec{F}_c| \end{bmatrix} = \begin{bmatrix} \sigma_{SG_{z-}} \\ \sigma_{SG_{z+}} \end{bmatrix} \quad (49)$$

3.3 Experimental setup

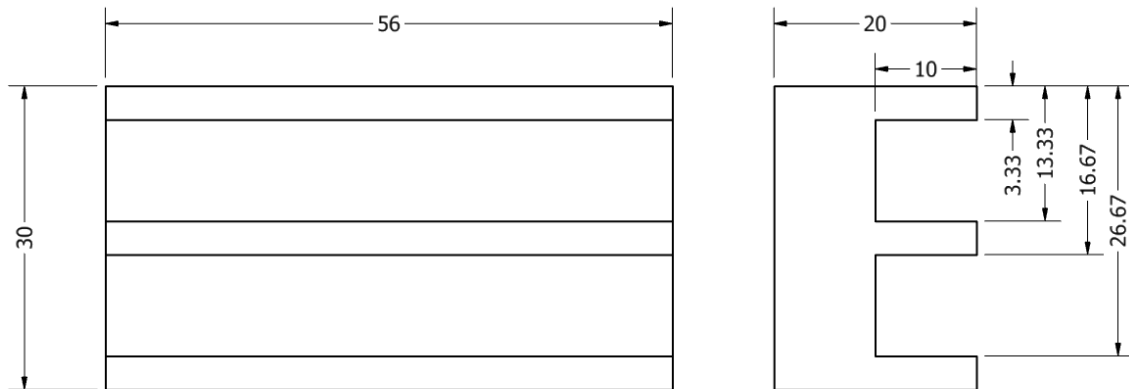
Established the mathematical model adopted to convert the acquired data to the interest force, the setup used in the tests is present in this chapter. The subsection 3.3.1 approaches the workpiece used in the tests, the subsection 3.3.2 deals with the cutting parameters used, and the subsection 3.3.3 explains about the data acquisition.

3.3.1 Workpiece

The design of the workpiece were made aiming to provide a permanent depth of cut a_p . To accomplished it, the cutting region was dimensioned with a width of 3,33 mm, around 1/3 of the tool cutting edge length. This way the experiment avoid the passive

force F_p . Three fillets with this width and a height of 10 mm were made, as shown by the graphic representation of the Figure 31. Two workpiece with identical geometries were used, both made of H13 steel without any treatment.

Figure 31 – Graphic representation of the workpiece.



Source: Author.

3.3.2 Cutting Parameters

To perform the machining tests, the cutting parameters for the shaping process were chosen looking for a maximization in the chip width h for future studies. Other factor determinant in the parameters choice, was the limitation of the machining tool. The diagram of Figure 32 shows the combinations of parameters possibles to be used in this machine.

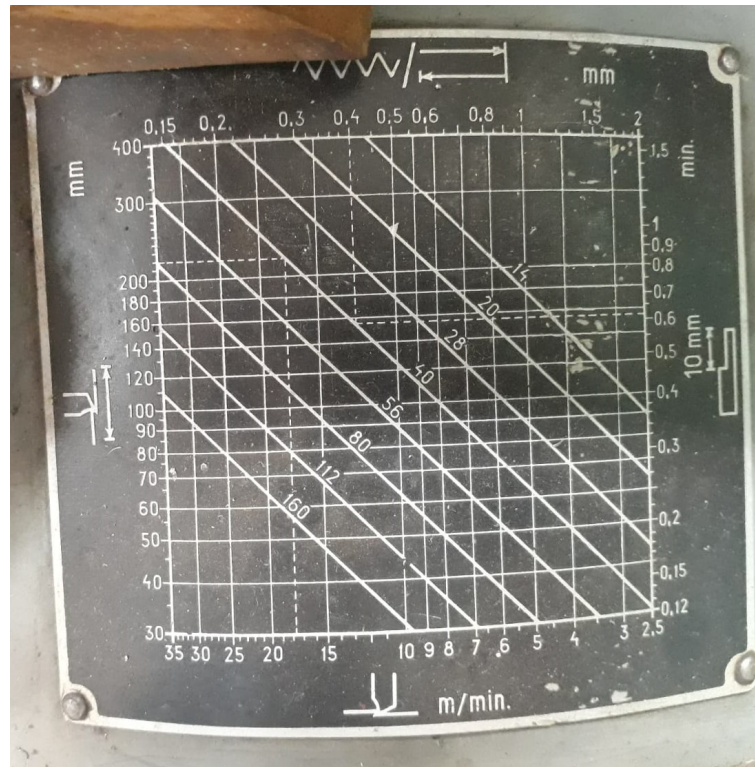
The tests were performed using five different tools, with geometries described in Table 3. Each tool has been hand sharpened. The cutting speed was fixed at 14m/min, and four different feeds f were used for all tools (0.5mm; 0.75mm; 1.00mm and 1.25mm). The depth of cut was initially fixed at 3.33mm, however due to the tool dynamic unstable behavior for this depth, it was changed to 0.2mm. To obtain the chip dimensions equals to these two last parameters, the cutting edge angle K_r was choose equals to 90° . All these parameters are shown in Table 4. The values L_Y and L_Z needed for the model adopted are shown in the Table 5 for each tool. None of the tools has chip break.

The reduction in depth of cut does produce passive force to the process, however due to it direction, regarding the strain gauges, the deflection caused by it is much smaller than the deflection caused by the active forces, hence it is assumed negligible.

Table 3 – Tools used in the tests.

Tool name	NEG2	NEG1	NEU0	POS1	POS2
Rake angle (γ_o)	-8.6°	-5°	0°	5°	8.6°
Clearance angle (α_o)	6.7°	13.1°	5.7°	10.2°	10.9°

Figure 32 – Diagram of cutting parameters combinations possible. Diagram available in the own machine.



Source: Author.

Table 4 – Cutting parameters.

Parameter	Value				
Tool	NEG2	NEG1	NEU0	POS1	POS2
Cutting edge angle (κ_r)	90°				
Cutting speed ($ \vec{v}_c $) [m/min]	14				
Depth of cut (a_p) [mm]	0,2				
Feed (f) [mm]	0.5	0.75	1.00	1.25	

Table 5 – Lever lengths.

Variable	Value				
Tool	NEG2	NEG1	NEU0	POS1	POS2
L_Y [mm]	106,58	107,16	101	102,7	103,2
L_Z [mm]	-0,15*	1,17	3	4,14	4,95

*The negative sign indicates the cutting edge is located behind the neutral axis for this tool.

Although the theory points to a feed equals to the uncut chip thickness ($f = h$), for cutting edge angle κ_r equals to 90°, the feed used as input does not provides an uncut chip thickness equals to it for the shaping process. It occurs, perhaps, due to imprecisions in the feed mechanism of the shaping machine. To suppress this difference, after each

section of cut, the filled height was measured using a caliper with resolution of 0,05mm. The differences of height were then divided by the total number of cuts of each section, allowing this way the correct determination of the uncut chip thickness.

Each variable combination of the Table 4 were used to cut the workpiece during sessions of 240 seconds. Since the shaping machine needs some time working until its stabilization at the correct parameters, only the eight middle cuts of each section were considered. For most of sessions the machine presented a considerable stabilization before and after eight middle cuts, hence for these cases there are more cuts. The number of cuts used per parameters combination is shown in Table 6.

Table 6 – Number of samples per variables combination. Cutting speed v_c , depth of cut a_p , and cutting edge angle κ_r were not changed.

Feed (f)	Tool				
	NEG2	NEG1	NEU0	POS1	POS2
0.50 [mm]	16	21	8	8	16
0.75 [mm]	15	20	12	14	8
1.00 [mm]	8	20	14	15	16
1.25 [mm]	22	13	15	21	15

3.3.3 Data acquisition

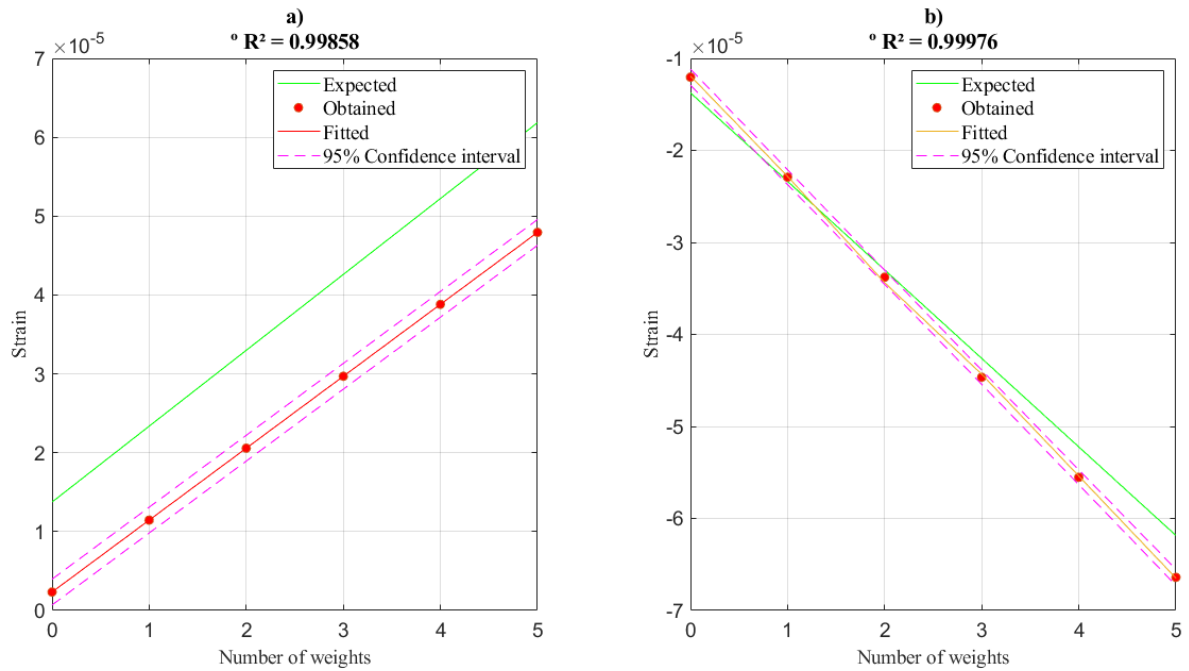
To stick the strain gauges in the tool holder, the glue points were sanded in a circular pattern, then it where cleaned using isopropyl alcohol. The sensors were bonded using a glue composed by ethyl 2-cyanoacrylate. After half hour the strain gauges were protected from the environment with layer of epoxy glue. The strain gauges terminals were protected using insulating tape. Then nine wires from a standard 10 way cable were weld to the strain gauges terminals. These wires were connected to the acquisition system.

During the cutting tests the strain measured by the strain gauges were acquired using the NI9237 module in a chassi cDAQ-9178 from National Instruments. A script in the software LabView was used for computing and write in parallel the data of the two pair of strain gauges, each pair connected to the module in a half bridge configuration. Inside the script, the software NiMax is used for the data acquisition. The software allows the direct acquisition of the strain value, in way that the manual conversion between the bridge voltage and the strain is not need. Both half bridges were supplied with a excitation voltage of 7.5V and were calibrated using a shunt circuit. 1000 sample per seconds was used as sample rate.

The data obtained by the LabView script was uploaded to a series of scripts in the software MatLab R2021a. These scripts applies filters using moving mean to remove the signal noise and also calculate the machining forces of interest as well as other interest variables using the modelling presented here. The moving mean used a window with 208 points, sufficient quantity to remove the noise.

Before the test performance with the tools, a test calibration was performed with each tool, in order to obtain the correction curve for the strain acquisition. This calibration were made fixing the tool holder in an horizontal position and then five known weights of steel (with a mass equal to 12,350kg) were attached one by one to the edge of the tool holder-tool assembly. Then five strain for each weight plus one, for no weights, were fitted and the resulting curve were compared with the expected curve (obtained analytically). These curves were plotted for each tool and are shown by the Figures 33, 34, 35, 36 and 37. A large bucket of 2,750kg was used to attach the weights to the assembly. Important to highlight that this calibration only covers the bending deformation.

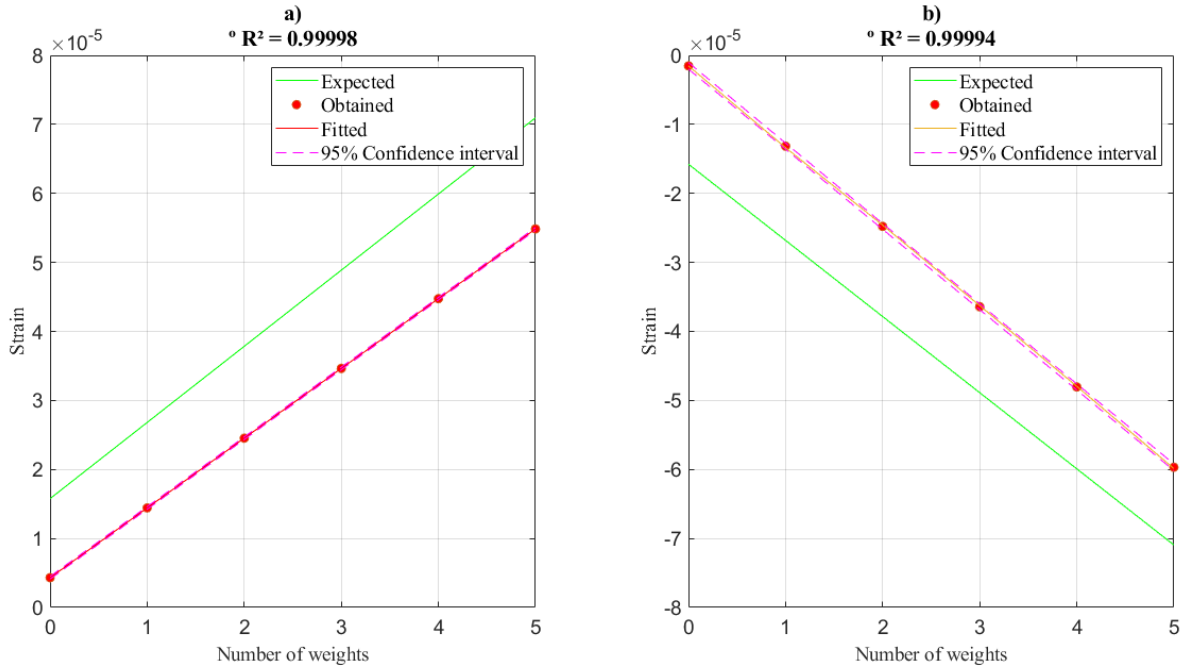
Figure 33 – Correction curve for strain calibration: a) Expected and obtained curves for front face strain gauge; b) Expected and obtained curves for back face strain gauge. Tool NEG2.



Source: Author.

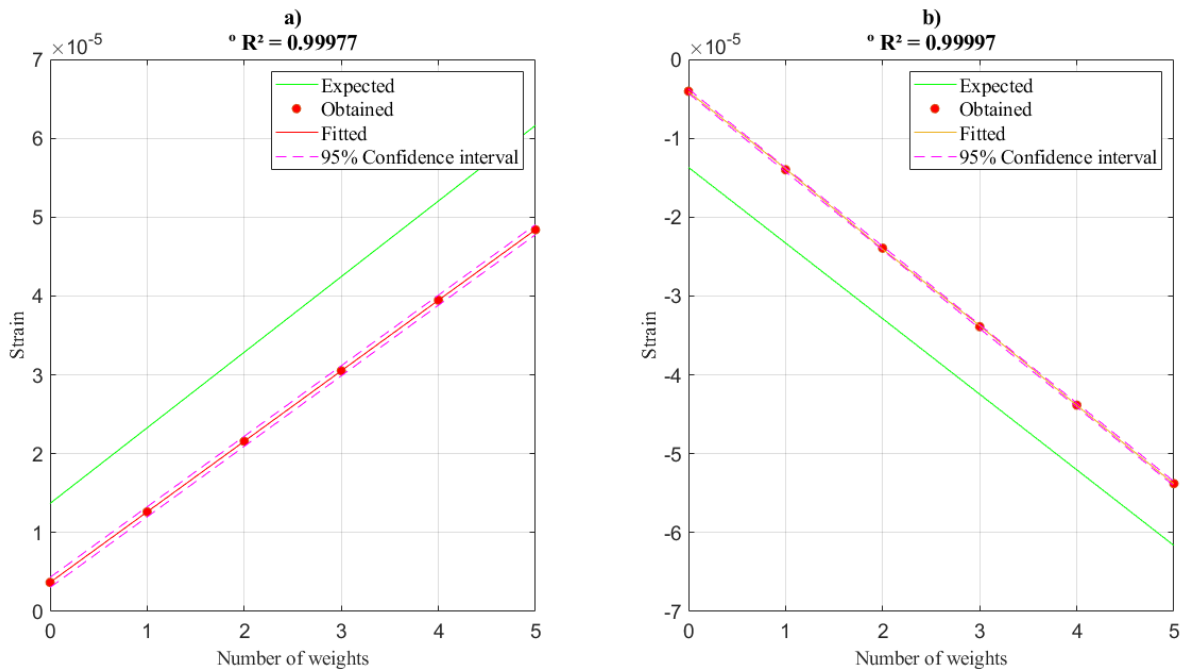
The line coefficients of the difference between the expected strain and obtained strain were exported to correct the strain from the actual machining tests. Notice that all the fits reach a R^2 higher than 0,99 which points to the correct read of strain by the sensors.

Figure 34 – Correction curve for strain calibration: a) Expected and obtained curves for front face strain gauge; b) Expected and obtained curves for back face strain gauge. Tool NEG1.



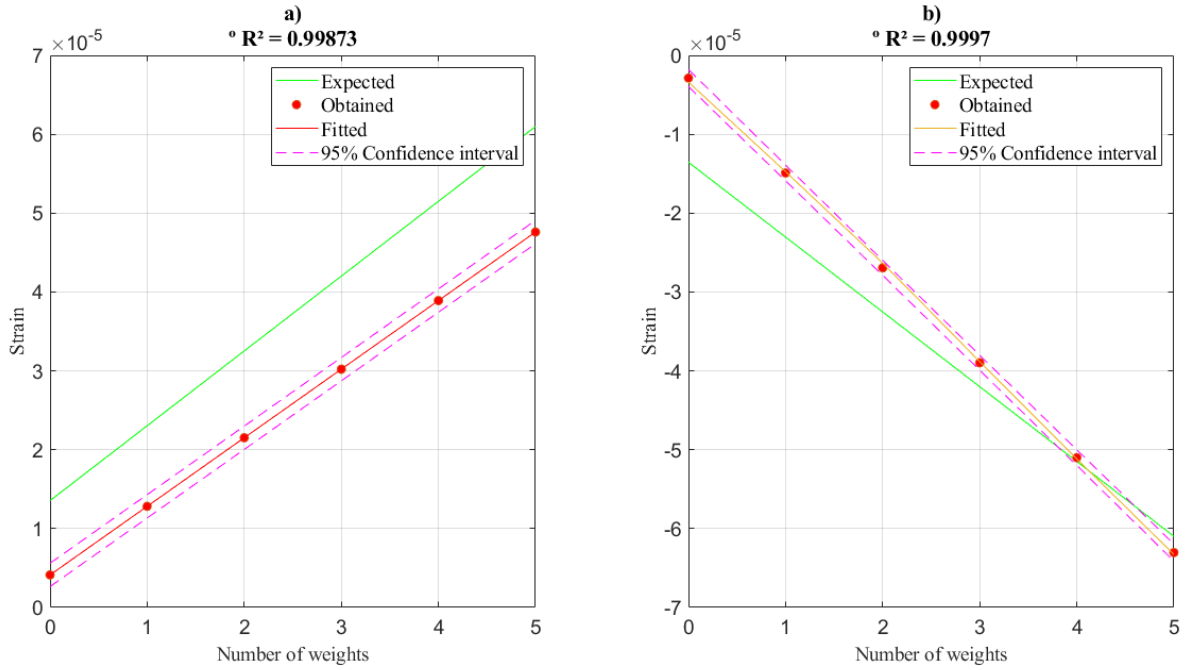
Source: Author.

Figure 35 – Correction curve for strain calibration: a) Expected and obtained curves for front face strain gauge; b) Expected and obtained curves for back face strain gauge. Tool NEU0.



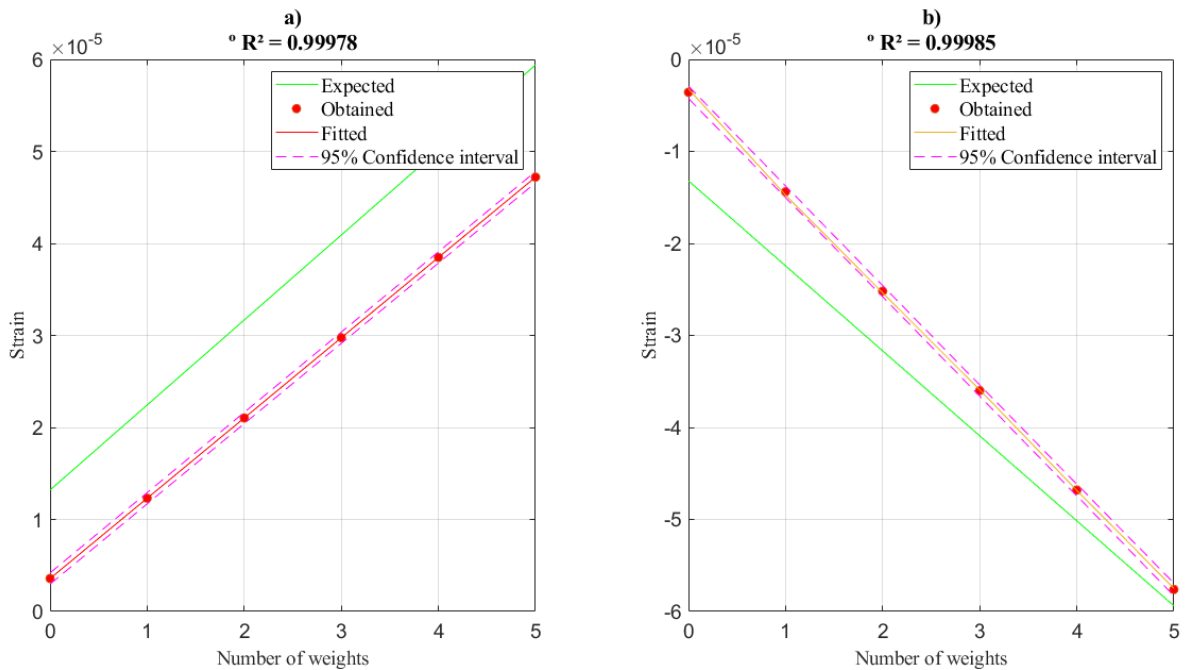
Source: Author.

Figure 36 – Correction curve for strain calibration: a) Expected and obtained curves for front face strain gauge; b) Expected and obtained curves for back face strain gauge. Tool rake angle γ_o : 5° .



Source: Author.

Figure 37 – Correction curve for strain calibration: a) Expected and obtained curves for front face strain gauge; b) Expected and obtained curves force back face strain gauge. Tool rake angle γ_o : 8.6° .



Source: Author.

4 RESULTS

In this chapter the results obtained based on the experimental goals for this monograph are present. First a verification of convergence between the results obtained by the strain gauges and numerical simulation is present. The second section shows the results for the active forces in the shaping process. The third and last section evaluates the Kienzle's constants.

4.1 Strain convergence

In order to verify the analytical model efficiency, and check if the strain gauges were correctly bonded, a new set of numerical simulations using FEM was performed, using the same model presented in 3.2.4. These simulations were performed using actual forces as input and the strains in the strain gauge region as output. These forces were obtained from the analytical model, using actual strains measured.

The simulation intend is to compare the strain measured with the strain obtained by FEM technique. If these strains converge to the same value, it means that the analytical model is converting correctly the strains into forces, and hence that the strain gauges were properly bonded.

For the simulation, the forces obtained for the tool NEU0 (see 4.2), were used as input, and the strains at the strain gauges region were taken as output. These values were compared to the strain measured, as shown by the Table 7.

Table 7 – Comparison between measured strains and simulation strains. Assembly with neutral tool.

Feed (f)	Simulated strain		Measured strain		Ratio (Measured/Simulated)	
	Front Face	Back Face	Front Face	Back Face	Front Face	Back Face
0.50 [mm]	2.816E-06	-6.601E-06	2.278E-06	-6.408E-06	0.9687	0.9708
0.75 [mm]	4.544E-06	-1.024E-05	4.429E-06	-9.930E-06	0.9746	0.9701
1.00 [mm]	3.604E-06	-9.984E-06	3.498E-06	-9.712E-06	0.9707	0.9728
1.25 [mm]	3.412E-06	-1.100E-05	3.319E-06	-1.071E-05	0.9728	0.9743

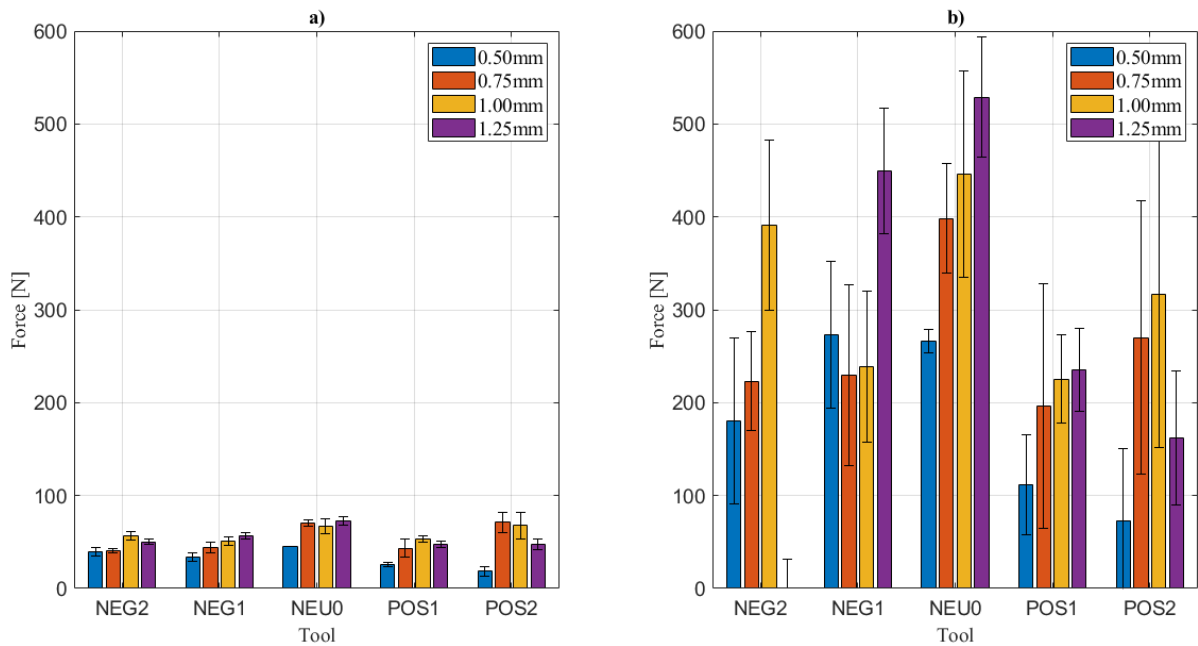
Since the measured strain represents around 97% of the expected strain (the actual strain, if it is considered the numerical simulation accurate enough), is reasonable both analytical model and strain gluing be considered correct. The values of R^2 for the calibration curves, presented in 3.3.3, reinforces this consideration.

4.2 Active machining forces

After the strain acquisition, the data were processed in a MatLab script described in section 3.3.3 which displays the results for the cutting force \vec{F}_c and feed force \vec{F}_f . The script also calculates the active force \vec{F}_a . The results for the feed and cutting force are displayed in Figure 38. For the active force \vec{F}_a the results are shown in Figure 39. Although these results contemplates all combination of variables proposed, it is necessary to notice the reservation present in 3.3.2 regarding the actual relation between the feed f and the uncut chip thickness h . The results considering this difference are shown below in Figure 41.

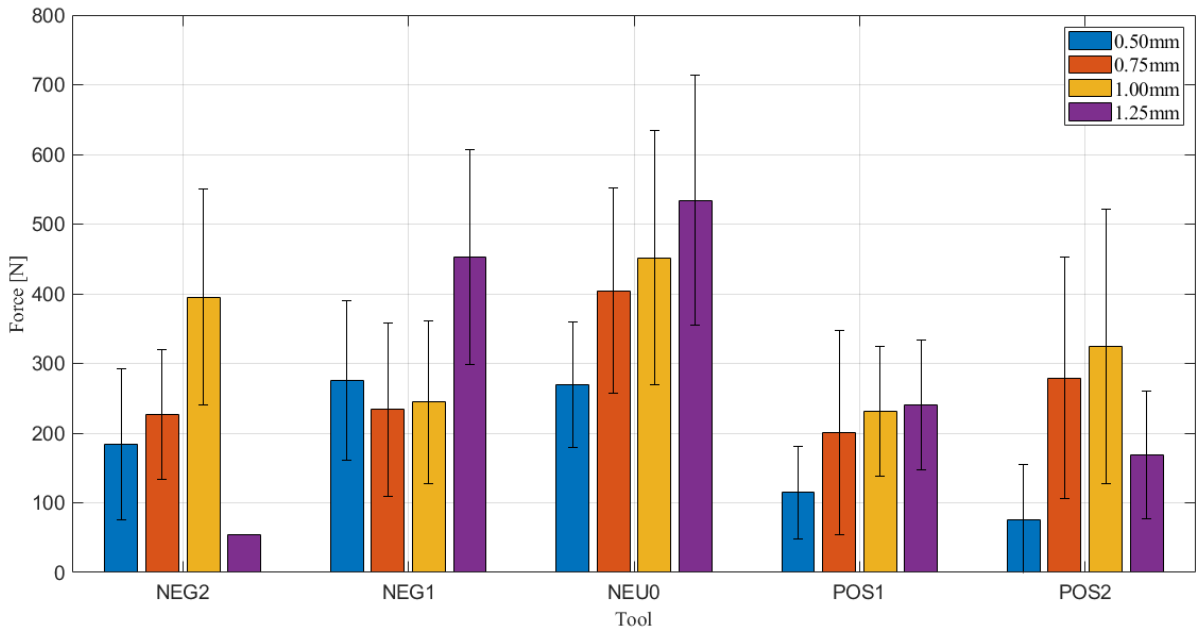
These results are the mean of cuts performed for each variable combination. The number of cuts per combination was presented in the Table 6. The error bar present on figures represents the uncertainly propagation (Carried from strains standard deviation).

Figure 38 – Active forces measured. Each bar represents a feed f . a) Cutting force \vec{F}_c ; b) Feed force \vec{F}_f .



Source: Author.

The first thing to be analysed is the cutting force for the tool NEG2 with feed f of 1,25mm. This result is not shown in Figure 38 due to its value computed. The strain measured for this parameter leads to a negative value of cutting force with magnitude equal to -20N. This negative value is perhaps due to the adhesion between the tool and workpiece, adhesion strong enough to pull the tool. The occurrence of this attachment may be associated with the extremism of parameters, i.e. the major value of feed with the most negative rake angle, two conditions which increase the cutting and feed forces (KLOCKE,

Figure 39 – Active force \vec{F}_a measured.

Source: Author.

2013). This hypothesis regarding the adhesion was not verified in this monograph, being study object for future studies.

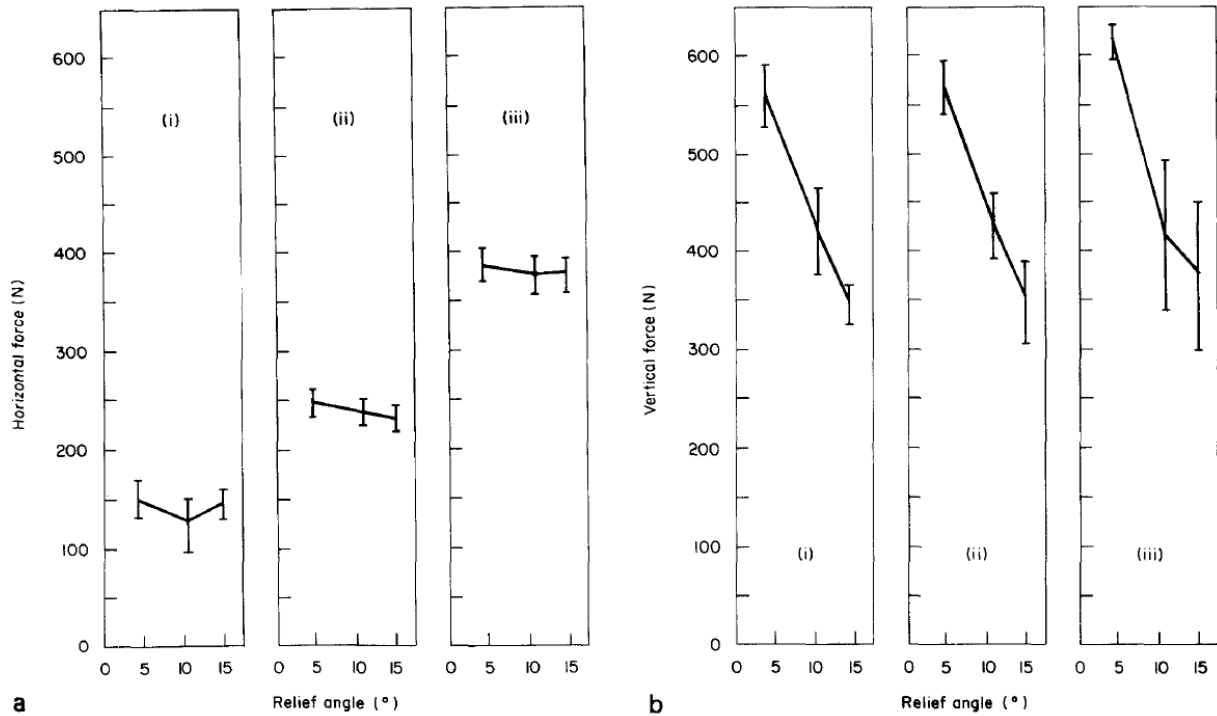
The notable unexpected result is the feed force \vec{F}_f being higher than the cutting force \vec{F}_c . Usually the cutting force \vec{F}_c is the major component of the active force \vec{F}_a (FERRARESI, 1970), but feed force \vec{F}_f being the major component was already reported in literature. Koplev, Lystrup e Vorm (1983) measured the active machining forces for fiber carbon machining, using tools with rake angles γ_o equals to 0° , 5° and 10° in a shaping machine, and all cut were performed in a direction parallel to the fibers. These tests found feed forces \vec{F}_f higher than the cutting forces \vec{F}_c , around four to ten times, for all cutting parameters used.

Moreover, Koplev, Lystrup e Vorm (1983) results presented a direct relation between the feed force \vec{F}_f and the clearance angle α_o , opposing the literature, as shown in Figure 40. Note that the increase in the clearance angle α_o leads to a decrease in the feed force \vec{F}_f .

In order to evaluate a possible influence of the clearance angle α_o in the results of this monograph, the Figure 41 shows the active forces versus the uncut chip thickness h presenting the clearance angle α_o of each tool.

Analysing the Figure 41 it is possible to note some relation between the clearance angle α_o and the feed force \vec{F}_f . The neutral tool NEU0 which has the minor clearance angle α_o presented the higher feed forces values even with the minor uncut chip thickness h , converging with the results obtained by Koplev, Lystrup e Vorm (1983).

Figure 40 – Cutting force \vec{F}_c (referred as “horizontal force” by authors) and feed force \vec{F}_f (referred as “vertical force” by authors) versus the clearance angle α_o (referred as “relief angle” by authors). a) Cutting force \vec{F}_c ; b) Feed force \vec{F}_f . (i) $h = 0,05\text{mm}$, $V_c = 48,6\text{m/min}$, $\gamma_o = 15^\circ$; (ii) $h = 0,1\text{mm}$, $V_c = 36\text{m/min}$, $\gamma_o = 15^\circ$; (iii) $h = 0,2\text{mm}$, $V_c = 26,4\text{m/min}$, $\gamma_o = 15^\circ$.



Source: Koplev, Lystrup e Vorm (1983).

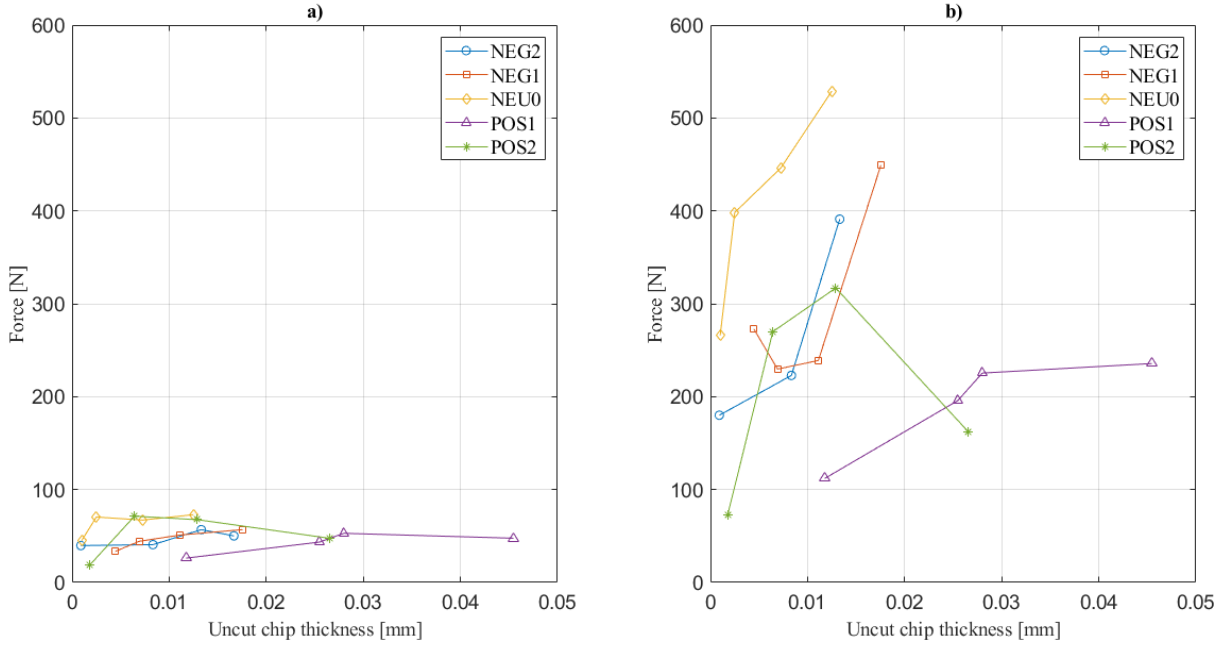
Since the worn tool is not a perfect edge, i.e the flank face touch the workpiece by an infinitesimal area and not only by the cutting edge, this leads to a friction between these parts, increasing the feed force \vec{F}_f by about 66% as described by Spaans (1967). A hypothesis correlating this effect to the increase in the feed force \vec{F}_f with the decrease in clearance angles α_o in e shaping processes is proposed: Minor clearance angles α_o provides more contact area between the workpiece and flank face, leading to the increment in feed force \vec{F}_f .

Following the analysis, after the tool NEU0, the tools with negative rake angle NEG2 and NEG1 presents the highest values for uncut chip thickness h around than 0,01mm. However, the tool POS2, which has the highest value of rake angle, shows it self as an anomaly around this value, since it presents two points with feed force higher than the tool NEG1.

For the cutting force F_c the results considering the different tools were pretty similar to each other, and does not present a high variation with the increase of the uncut chip thickness h .

Other approach to the unusual relation between the values of the feed and cutting forces, it is due to the formation of build-up edge in the tool. This phenomenon occurs at

Figure 41 – Active forces measured versus uncut chip thickness h . a) Cutting force \vec{F}_c ; b) Feed force \vec{F}_f .



Source: Author.

low cutting speeds, and it is result of material adhesion from workpiece in the tool cutting edge. Wallace e Boothroyd (1964) points to the risk of build-up edge in tools with rake angle γ_o minor than 15° performing cutts with cutting speeds around 10 to 20m/min.

During the tests performed for this work, the build-up edge formation was verified in almost all cut sections, which can leads to the unexpected values of forces obtained. The Figure 42 shows a wear in the neutral tool caused by the build-up edge formation. The cutting speed for the tests was not increased because it increase was leading to an unstable cutting, i.e the tests were presenting higher leves of vibration.

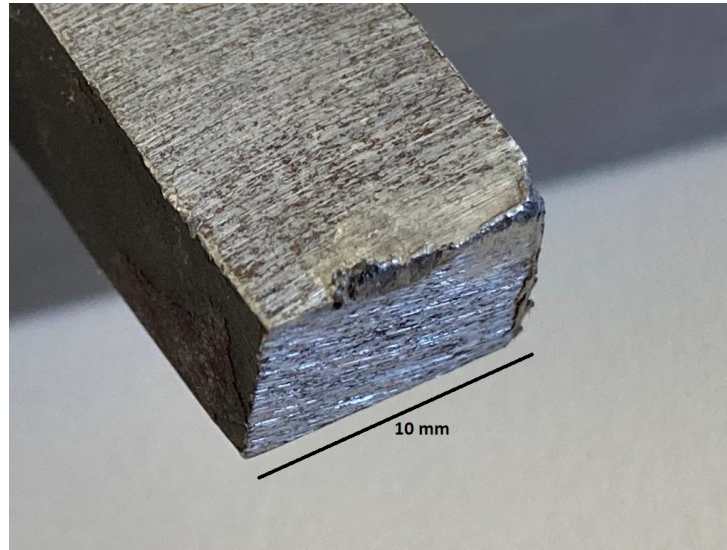
4.3 Shear angle and Kienzle's constants

Based on the results obtained for active force components, it is possible to determine the shear angle Φ and the Kienzle's constants $K_{s,1}$ and z for the cutting force \vec{F}_c and $K_{f,1}$ and y for the feed force \vec{F}_f .

To determine the shear angle, the equations presented in Merchant's model (see 2.3) were used. The shear angles Φ for each combination of parameters are shown in Table 8.

Once again it is important to highlight that both the Merchant's model used for the shear angle Φ determination and the Kienzle's model are applied for the orthogonal cutting theory, which does not consider the formation of build-up edge in the process. Due to this, the values presents in Table 8 are an extrapolation of the theory, and may diverge

Figure 42 – Neutral tool Wear due to build-up edge formation.



Source: Author.

Table 8 – Shear angle Φ per variables combination.

Feed (f)	Tool				
	NEG2	NEG1	NEU0	POS1	POS2
0,50 [mm]	6,25°	3,49°	4,83°	6,59°	7,04°
0,75 [mm]	5,17°	5,45°	5,02°	6,26°	7,41°
1,00 [mm]	4,14°	6,03°	4,28°	6,61°	6,02°
1,25 [mm]	-	3,61°	3,93°	5,71°	8,17°

from the actual values.

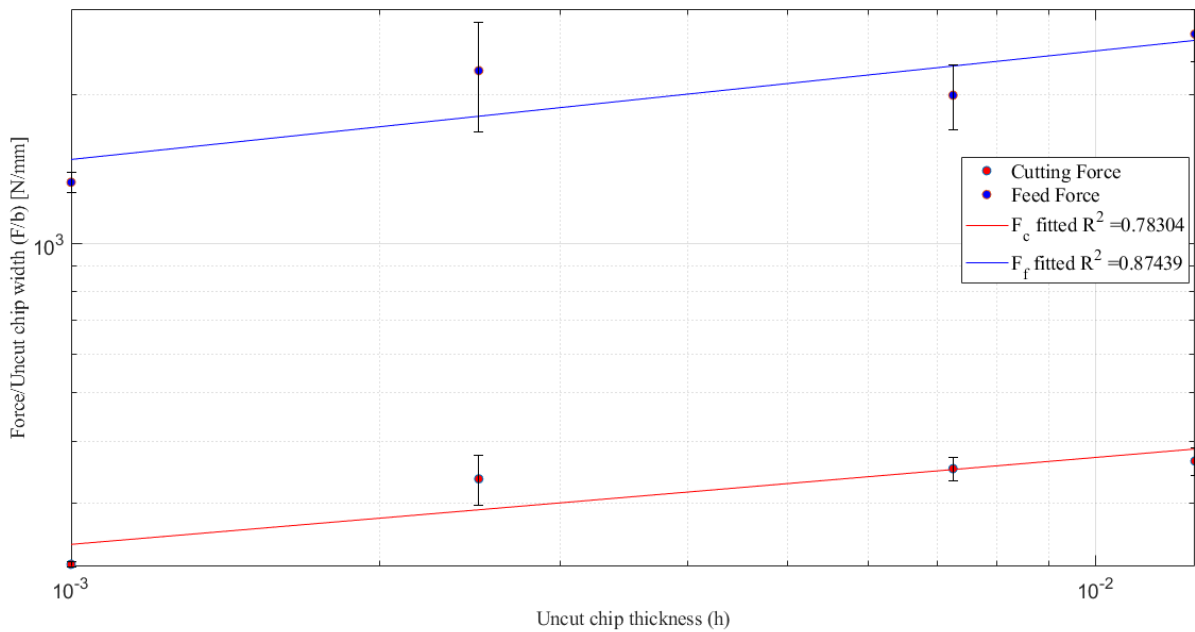
To determine the Kienzle's constants, the data for the tool NEU0 were used, the ratios between the forces and the chip width were plotted versus the uncut chip thickness h in a loglog graph, and the Equation 19 was applied. The log-log graph is shown in Figure 43 and the constants values in Table 9. In this table, $K_{i,1}$ represents the specific cutting pressure $K_{s,1}$ for the first row and $K_{f,1}$ for the second row. The force gradient is z for the first row and x for the second row.

Table 9 – Kienzle's constants experimentally determined for the neutral tool.

Constant	$K_{i,1}$ [N/mm ²]	Force gradient
Cutting force \vec{F}_c	830,7	0,8248
Feed force \vec{F}_f	6691,1	0,7811

Machado et al. (2009) presents the values for the Kienzele's constants for different materials in the milling processes. These values for high alloy steels are 1950 N/mm² for the specific cutting pressure $k_{s,1}$ and 0.25 for the force gradient z . Considering that these values were determined using a different processes than the employed in this monograph, the values obtained here for the specific cutting pressure $k_{s,1}$ are reasonable.

Figure 43 – Linearized forces for the Kienzle’s constants determination.



Source: Author.

The high values found in this monograph for the forces gradient z and x points to a low dependence in the tests between the active forces and the uncut chip thickness h , which can be visualized in Figure 41 a), where for all tools the increment in the uncut chip thickness h does not change significantly the cutting force \vec{F}_c . In Figure 41 b) although some apparently relation between the increase in force for the tool NEU0 the other tools does not present a clearly relation with the increment of uncut depth of cut h .

Although the reasonable results for the cutting pressure, the results for the force gradient z , diverges considerably from the determined by the literature, perhaps due to the presence of build-up edge in the tests, since Machado et al. (2009) warns about the need of use high cutting speeds to avoid the build-up edge formation, not allowing the use of the Kienzle’s model for this cases.

5 CONCLUSION

After a solid presentation regarding the cutting theories (Orthogonal cutting theory, Merchant's model and Kienzle's model), this monograph seeks for the creation of a tool holder able to measure the active cutting forces and then validate these theories. In order to perform this design, this monograph also presents an integrating look joining the machining studies with the materials mechanics theory.

The results regarding the convergence between the expected strain based in numerical simulation via FEM and the strains measured points to a success in the propose of force measurement, and hence in the analytical model used to convert the measured strains to the machining forces of interest.

The validation of the theories however does not succeed as good as the force measurement. Due to the cutting parameters used in tests, the cutting tool in some cutting sessions presented build-up edge formation, being it probably the reason for the discrepant values, deserving this way future studies. However, an extrapolation of these theories was made and then the main variables and constants presents in each theory were calculated.

Regarding the didactic purpose of this work, joining the experimental tests with the theories presented here, this monograph shows a good approach to the study of machining forces in the mechanical engineering course, integrating it with others subjects, such as materials mechanics and instrumentation. In general the monograph accomplished with the proposed goals.

5.1 Future works

Since the validation of the theories does not succeed as the expected, for future works some setup parameters will be modified. These changes are listed below.

- Use of new cutting parameters, less extreme than used here;
- Workpiece fillets with a narrow width, in order to avoid passive forces;
- Narrow the tool holder width in order to obtain a more stable region;
- Decrease the tools length in order to provide a more stable dynamic behavior for the cut process;
- Calibrate the strain gauges considering bending and compression loads.

Additional to the force measurement, the chip formation can be studied deeper, regarding the thermal loads involved in the cutting process and also the vibration. The "Quick-stop" technique can also be applied. These new approaches can perhaps determinate the causes of the negative value for the maximum feed in the most negative tool.

REFERENCES

- Associação Brasileira de Normas Técnicas (ABNT). **Grandezas básicas em usinagem e retificação - Parte 1: Geometria da parte cortante das ferramentas de corte — Termos gerais, sistemas de referência, ângulos da ferramenta e de trabalho e quebra-cavacos.** 2013. Norma Técnica. Rio de Janeiro.
- BATHE, K.-J. **Finite Element Method.** [S.l.]: John Wiley & Sons, Inc., 2008.
- BEER, F. P. et al. **Mechanics of Materials.** 7. ed. New York, NY: McGraw-Hill Professional, 2014.
- BÄKER, M. Does chip formation minimize the energy? **Computational Materials Science**, v. 33, n. 4, p. 407–418, 2005. ISSN 0927-0256.
- DIN8580. **Manufacturing processes – Terms and definitions, division.** DIN 8580:2003. [S.l.]: Deutsches Institut Fur Normung, 2003.
- DIN8589. **Manufacturing processes – Terms and definitions, division.** DIN 8589:2003. [S.l.]: Deutsches Institut Fur Normung, 2003.
- FERRARESI, D. **Fundamentos da Usinagem dos Metais.** [S.l.]: Blucher, 1970. ISBN 9788521214199.
- GARRIDO, H. et al. Numerical modelling of orthogonal cutting: Influence of cutting conditions and separation criterion. **Journal de Physique IV (Proceedings)**, v. 134, 08 2006.
- HOFFMANN, K. **An Introduction to Measurement Using Strain Gages.** [S.l.]: Hottinger Baldwin, 1989.
- KIENZLE, O. Die bestimmung von kräften und leistungen an spanenden werkzeugen und werkzeugmaschinen. **VDI-Z**, v. 94, n. 11, p. 299–305, 1952.
- KLOCKE, F. **Manufacturing processes 1.** 2011. ed. Berlin, Germany: Springer, 2013. (RWTHedition).
- KOPLEV, A.; LYSTRUP, A.; VORM, T. The cutting process, chips, and cutting forces in machining cfrp. **Composites**, v. 14, n. 4, p. 371–376, 1983. ISSN 0010-4361.
- LALWANI, D.; MEHTA, N.; JAIN, P. Experimental investigations of cutting parameters influence on cutting forces and surface roughness in finish hard turning of mdn250 steel. **Journal of Materials Processing Technology**, v. 206, n. 1, p. 167–179, 2008. ISSN 0924-0136.
- MACHADO, A. et al. **Teoria Da Usinagem Dos Materiais.** [S.l.]: EDGARD BLUCHER, 2009. ISBN 9788521204527.
- MERCHANT, M. E. Mechanics of the metal cutting process. i. orthogonal cutting and a type 2 chip. **Journal of Applied Physics**, AIP Publishing, v. 16, n. 5, p. 267–275, maio 1945.

- MERCHANT, M. E. Mechanics of the metal cutting process. II. plasticity conditions in orthogonal cutting. **Journal of Applied Physics**, AIP Publishing, v. 16, n. 6, p. 318–324, jun. 1945.
- MOLINARI, A.; MOUFKI, A. The merchant's model of orthogonal cutting revisited: A new insight into the modeling of chip formation. **International Journal of Mechanical Sciences**, v. 50, n. 2, p. 124–131, 2008. ISSN 0020-7403.
- SPAANS, C. An exact method to determine the forces on the clearance plane. **Annals of the CIRP**, v. 15, n. 4, p. 463, 1967.
- UFSCAR. Pedagogical Project, **Projeto pedagógico cursode bacharelado em engenharia mecânica**. São Carlos, Brazil: [s.n.], 2013.
- WALLACE, P. W.; BOOTHROYD, G. Tool forces and tool-chip friction in orthogonal machining. **Journal of Mechanical Engineering Science**, SAGE Publications, v. 6, n. 1, p. 74–87, mar. 1964.
- ZVORYKIN, K. Work and stress necessary for separation of metal chips. **Proceedings of the Kharkov Technological Institute, Ukraine**, 1893.